
Since January 2020 Elsevier has created a COVID-19 resource centre with free information in English and Mandarin on the novel coronavirus COVID-19. The COVID-19 resource centre is hosted on Elsevier Connect, the company's public news and information website.

Biomaterials 59 (2015) 125–143

Contents lists available at ScienceDirect

Biomaterials

journal homepage: www.elsevier.com/locate/biomaterials

# Phytomolecule icaritin incorporated PLGA/TCP scaffold for steroid-associated osteonecrosis: Proof-of-concept for prevention of hip joint collapse in bipedal emus and mechanistic study in quadrupedal rabbits

Ling Qin [a, b, *, 1], Dong Yao [a, 1], Lizhen Zheng [a, 1], Wai-Ching Liu [a, 1], Zhong Liu [a], Ming Lei [c], Le Huang [a], Xinhui Xie [a], Xinluan Wang [a, b], Yang Chen [d, 2], Xinsheng Yao [e], Jiang Peng [a, f], He Gong [g], James F. Griffith [h], Yanping Huang [i], Yongping Zheng [i], Jian Q. Feng [j], Ying Liu [j], Shihui Chen [a], Deming Xiao [c], Daping Wang [d], Jiangyi Xiong [d], Duanqing Pei [k], Peng Zhang [b], Xiaohua Pan [l], Xiaohong Wang [m], Kwong-Man Lee [n], Chun-Yiu Cheng [a]

[a] Musculoskeletal Research Laboratory, Department of Orthopaedics & Traumatology, The Chinese University of Hong Kong, Hong Kong SAR, PR China
[b] Translational Medicine R&D Center, Institute of Biomedical and Health Engineering, Shenzhen Institutes of Advanced Technology, Chinese Academy of Sciences, Shenzhen, PR China
[c] Department of Orthopaedics, Peking University Shenzhen Hospital, Shenzhen, PR China
[d] Department of Orthopaedics, The Second People's Hospital of Shenzhen, Shenzhen, PR China
[e] Institute of Traditional Chinese Medicine & Natural Products, College of Pharmacy, Jinan University, Guangzhou, PR China
[f] Orthopaedic Research Institute, Chinese People's Liberation Army General Hospital, Beijing, PR China
[g] School of Biological Science and Medical Engineering, Beihang University, Beijing, PR China
[h] Department of Imaging and Interventional Radiology, The Chinese University of Hong Kong, Hong Kong SAR, PR China
[i] Interdisciplinary Division of Biomedical Engineering, The Hong Kong Polytechnic University, Hong Kong SAR, PR China
[j] Baylor College of Dentistry, Texas A&M University, Dallas, USA
[k] Guangzhou Institutes of Biomedical and Health, Chinese Academy of Sciences, Guangzhou, PR China
[l] Department of Orthopaedics, The First Peoples' Hospital, Shenzhen, PR China
[m] Department of Mechanical Engineering, Tsinghua University, Beijing, PR China
[n] Lee Hysan Clinical Research Laboratories, The Chinese University of Hong Kong, Hong Kong SAR, PR China

ARTICLE INFO

*Article history:*
Received 2 February 2015
Received in revised form
15 April 2015
Accepted 21 April 2015
Available online 15 May 2015

*Keywords:*
Steroid-associated osteonecrosis
Bipedal emus
Hip collapse
Bioactive composite porous scaffold
Phytomolecule icaritin

ABSTRACT

Steroid-associated osteonecrosis (SAON) may lead to joint collapse and subsequent joint replacement. Poly lactic-co-glycolic acid/tricalcium phosphate (P/T) scaffold providing sustained release of icaritin (a metabolite of Epimedium-derived flavonoids) was investigated as a bone defect filler after surgical core-decompression (CD) to prevent femoral head collapse in a bipedal SAON animal model using emu (a large flightless bird). The underlying mechanism on SAON was evaluated using a well-established quadrupedal rabbit model. Fifteen emus were established with SAON, and CD was performed along the femoral neck for the efficacy study. In this CD bone defect, a P/T scaffold with icaritin (P/T/I group) or without icaritin (P/T group) was implanted while no scaffold implantation was used as a control. For the mechanistic study in rabbits, the effects of icaritin and composite scaffolds on bone mesenchymal stem cells (BMSCs) recruitment, osteogenesis, and anti-adipogenesis were evaluated. Our efficacy study showed that P/T/I group had the significantly lowest incidence of femoral head collapse, better preserved cartilage and mechanical properties supported by more new bone formation within the bone tunnel. For the mechanistic study, our *in vitro* tests suggested that icaritin enhanced the expression of osteogenesis related genes COL1α, osteocalcin, RUNX2, and BMP-2 while inhibited adipogenesis related genes C/EBP-ß, PPAR-γ, and aP2 of rabbit BMSCs. Both P/T and P/T/I scaffolds were demonstrated to recruit BMSCs both *in vitro*

* Corresponding author. Department of Orthopaedics & Traumatology, The Chinese University of Hong Kong, 5/F, Clinical Science Building, Prince of Wales Hospital, Shatin, Hong Kong SAR, PR China.
*E-mail address:* lingqin@cuhk.edu.hk (L. Qin).
[1] These authors contributed equally to this work.
[2] Liaison for emu research in Shenzhen.

http://dx.doi.org/10.1016/j.biomaterials.2015.04.038
0142-9612/

and *in vivo* but a higher expression of migration related gene VCAM1 was only found in P/T/I group *in vitro*. In conclusion, both efficacy and mechanistic studies show the potential of a bioactive composite porous P/T scaffold incorporating icaritin to enhance bone defect repair after surgical CD and prevent femoral head collapse in a bipedal SAON emu model.



## 1. Introduction

Steroid-associated osteonecrosis (SAON) is a common orthopaedic problem following steroid treatment for many medical conditions such as rheumatoid arthritis, systemic lupus erythematosus, organ transplantation, asthma and severe acute respiratory syndrome [1–5]. Osteonecrosis (ON) mainly affects large joints, such as hip, that may subsequently progress to joint collapse requiring total joint replacement [3,6]. According to the Centers of Disease Control and Prevention of the United States, there were 464,452 total hip replacements performed in 2011 [7], in which ON accounts for around 10% of all cases [8]; the total hospitalization cost of hip joint replacements in US was estimated to be around US$8 billion in 2011 [7]. The prognosis of joint replacement in SAON patients is poor due most likely to impaired osteoblast, osteocyte and osteoclast functions with steroid use leading to impaired repair and osteogenesis as well as upregulation of adipogenic potential of bone mesenchymal stem cells (BMSCs) [9,10].

Our recent studies showed that phytochemical molecule icaritin, a metabolite derived from herbal Fufang which was developed for treatment of postmenopausal osteoporosis [11,12], could reduce SAON incidence by inhibiting both thrombosis and lipid deposition in rabbits [13]. We also showed icaritin was a unique phytomolecule capable of both promoting osteogenesis as well as inhibiting adipogenic differentiation of BMSCs [14,15]. As icaritin is a chemically stable exogenous phytomolecule, we were able to incorporate it into poly lactic-co-glycolic acid (PLGA) and tricalcium phosphate (TCP) to form a PLGA/TCP/icaritin composite porous scaffold using low-temperature rapid prototyping (RP) technology [16–18]. RP technology is becoming popular in musculoskeletal tissue engineering due to its ease, flexibility and reproducibility for manufacturing scaffolds closely mimicking structural defects with complex structures [19,20]. The composite scaffold was tested for its efficacy as a bone defect filler for enhancing bone defect repair in both established SAON and segmental ulnar defect rabbit models; the presence of icaritin significantly induced more new bone formation in the defects, attributed to the sustained release of the bioactive phytomolecule icaritin from the composite scaffold [18,21,22]. However, unlike end-stage ON in human beings, rabbit is a quadrupedal animal so that no hip joint collapse would occur after SAON induction in our previous studies and also others.

Applying a recently established bipedal emu SAON model with femoral head collapse similar to that typically observed in patients [23], this study was designed to test the ability of our unique PLGA/TCP/icaritin scaffold to enhance bone defect repair within a bone tunnel after surgical CD and to prevent femoral head collapse. The underlying mechanisms associated with the potential enhancement of osteogenesis and anti-adipogenesis involving BMSCs were also evaluated both *in vitro* and *in vivo* using our established cost-effective quadrupedal rabbit SAON model [9,10,18,24], together with studying the signaling pathways involved. A flowchart describing the entire study is presented in Fig. 1. This proof-of-concept pre-clinical study is necessary before making a recommendation for conducting clinical trials and future clinical applications.

## 2. Materials and methods

### 2.1. Composite scaffold fabrication

PLGA/TCP composite scaffolds with or without incorporating icaritin were fabricated using a low-temperature RP machine (CLRF-2000-II; Tsinghua University, Beijing, China) based on our established protocol [18,22,25]. Briefly, PLGA (75:25) (Shandong Institute of Medical Instruments, Jinan, China) was dissolved in 1,4-dioxane before TCP (Beijing Organic Chemical Plant, Beijing, China) was added to form a uniform paste with a ratio of 4:1 (w/w of PLGA/TCP) by vigorous stirring overnight. Icaritin was added 320 mg per 100 g PLGA/TCP to form the PLGA/TCP/icaritin scaffold (P/T/I) based on our previous validation study [22]. Then the paste was spurted out layer-by-layer at a thickness of 500 μm and distance of 500 μm (default pore size) by a computer-driven nozzle to form a homogenous cubic porous scaffold. A demonstration scaffold measuring $20 \times 20 \times 20$ mm$^3$ is shown in Fig. 2A. The exact size of the scaffold for each study was mentioned in the corresponding section below. The fabrication temperature in the production chamber was set at −28 °C ensuring bioactivity of the phytomolecule icaritin. The scaffold was then lyophilized for 24 h and sealed in a plastic bag before evaluation or implantation. For comparison, pure PLGA/TCP scaffold (P/T) was also produced in a similar fashion. All chemicals were purchased from Sigma–Aldrich (St. Louis, MO, USA) unless specified.

### 2.2. Emu efficacy study

#### 2.2.1. Emu grouping and treatment

Adult male emus of 24 months old used for this study were provided and kept in Shenzhen Emu Institute, where these emus received food and water *ad libitum* (Supplementary Fig. S1). The animal experimental protocol was approved by the Research Ethics Committee of Shenzhen Second Peoples' Hospital (Licence No. 2009–001). Following the established protocol for inducing SAON in emus [23], 15 emus were treated with a combination of lipopolysaccharide (LPS) (*Escherichia coli* O111:B4; Sigma–Aldrich) and methylprednisolone (MPS) (Pharmacia & Upjohn, Peapack, NJ, USA). The animals were injected with LPS (8 μg/kg body weight) intravenously twice at day 0 and day 4, and MPS (10 mg/kg body weight) intramuscularly injected at day 8, 10 and 12.

#### 2.2.2. Surgical CD and scaffold implantation

Twelve weeks post-induction of SAON, emus were anesthetized with xylazine (2 mg/kg body weight) and ketamine (50 mg/kg body weight) injection intramuscularly. A skin insertion was created to expose the greater trochanter. Core decompression of 6 mm diameter was performed from the greater trochanter along the axis of the femoral neck bilaterally. The tunnel direction was in the mid-axis of the femoral neck. A pin, which was positioned 5 mm away from the endosteal surface of the femoral head, was inserted to guide the drilling of the bone tunnel. Using a 4 mm diameter hollow bone drill, a bone tunnel was created from the greater trochanter towards the femoral head with reference to the pin and

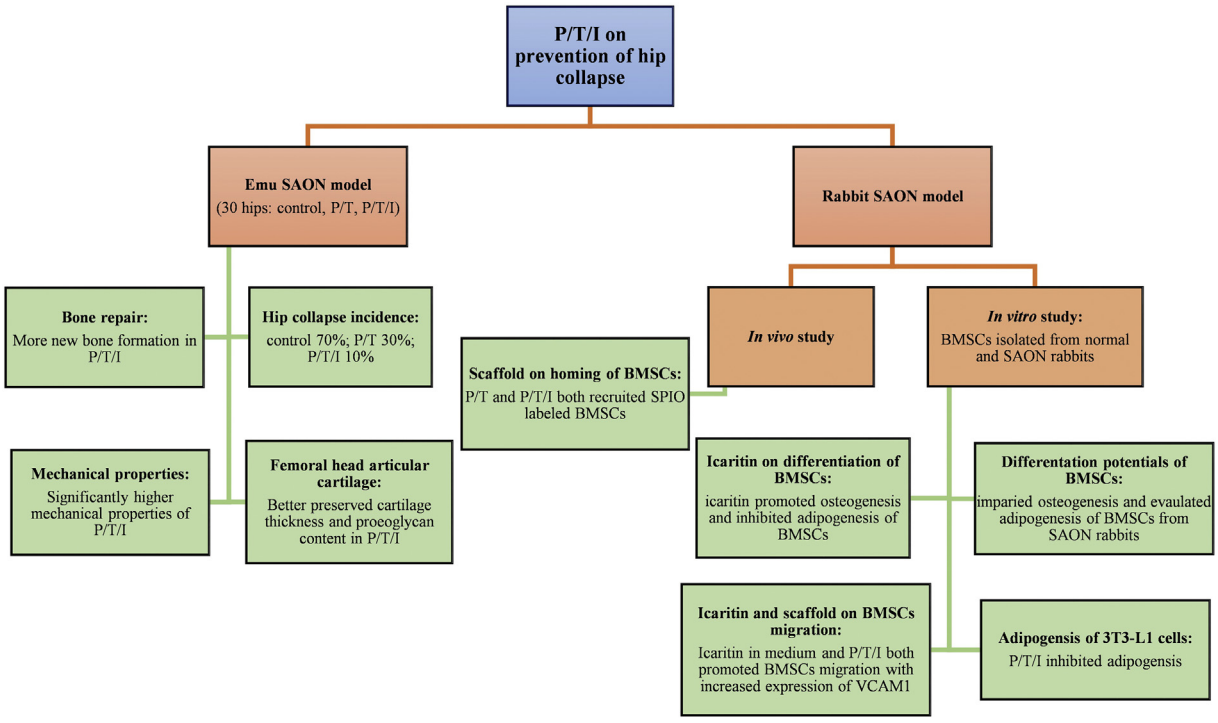


**Fig. 1.** A flowchart describing the entire study.

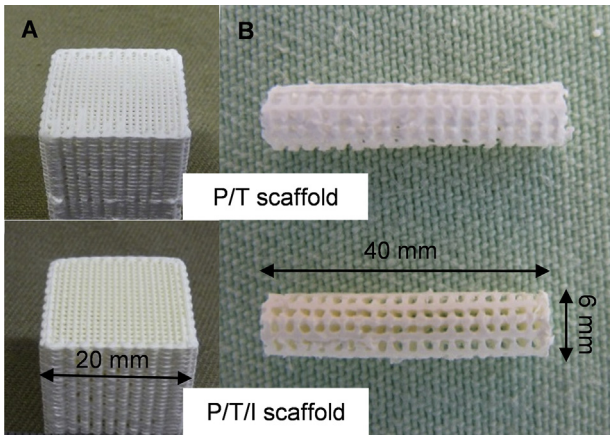


**Fig. 2.** (A) Macroscopic appearances of the fabricated P/T scaffold (upper, white in color) and P/T/I scaffold (below, yellowish, attributed by the color of icaritin) in their original forms. (B) Cylindrical scaffolds of P/T (upper, white in color) and P/T/I (below, yellowish) prepared for emu implantation. (For interpretation of the references to color in this figure legend, the reader is referred to the web version of this article.)

anatomical landmarks (depth of bone tunnel = 40 mm). This 4 mm tunnel was expanded with a 6 mm diameter drill bit. The 30 hips of the 15 SAON emus were randomly assigned to one of following three groups: P/T/I group (n = 10), P/T group without icaritin used as vehicle control (n = 10) and empty control group without scaffold implantation (n = 10). The scaffolds were prepared into cylinders of 6 mm diameter (Fig. 2B), and were press fitted into the bone tunnels (Supplementary Video S1). Five additional emus were assigned to normal control group (n = 10) without SAON induction and CD surgery, which the emus were euthanized one day after scaffold implantation as baseline for comparison.

Supplementary video related to this article can be found at http://dx.doi.org/10.1016/j.biomaterials.2015.04.038.

### 2.2.3. MRI imaging

Magnetic resonance imaging (MRI) (Magnetom Trio 3T MRI System; Siemens, Germany) with a phased-array body coil was performed to determine successful establishment of SAON 12 weeks after SAON induction, and also to confirm the correct position of the bone tunnel and placement of the cylindrical scaffold. For facilitating *in vivo* imaging examination, a specific posture device was used to obtain a highly reproducible emu position during MRI scanning (Supplementary Fig. S2). Coronal turbo spin-echo T2-weighted fat-saturated images (4000 ms repetition time; 96 ms echo time) were obtained with a slice thickness of 3 mm, an interslice distance of 0.3 mm providing a field of view of 300 mm × 300 mm and a matrix of 320 × 320 pixels.

### 2.2.4. Gross anatomical evaluation

Twelve weeks post core-decompression and implantation, emus were euthanized and the femora were collected. The collapsed region at the femoral head was digitally imaged and evaluated visually for surface subsidence of the articular cartilage.

### 2.2.5. Ultrasound imaging and indentation test

Ultrasound imaging and water-jet ultrasound indentation test were performed to measure the thickness and stiffness of emu femoral head cartilage using our established protocol (Supplementary text) [26,27]. Briefly, the thickness of the cartilage was calculated by averaging the distance of cartilage to the subchondral bone on three images obtained by B-mode ultrasound scanning (Supplementary Fig. S3). A water-jet ultrasound indentation probe (Supplementary Fig. S4A) was used to measure the stiffness of the cartilage; the water-jet compressed the cartilage and the deformation was measured by an ultrasound probe installed at the tip (Supplementary Fig. S4B). The experimental details of ultrasound imaging and indentation were provided in the supplementary text together with relevant references.

*2.2.6. Micro-CT imaging*

After water-jet indentation test, the proximal femora were fixed in 70% ethyl alcohol for bone scanning using a high-resolution peripheral computed tomography (HR-pQCT, Scanco Medical, Brüttisellen, Switzerland) with a source voltage of 70 keV and current of 114 μA. The entire scan length of 40 mm with a spatial resolution of 40 μm was used for animal experimental studies. For separating the signals of the mineralized tissue from the background signal, noise was removed using a low-pass Gaussian filter (sigma = 2.5, support = 2), and mineralized tissue was then defined at a threshold of 85 Hounsfield units [28,29]. Three-dimensional (3-D) images of the femoral heads were reconstructed. Articular surface collapse was defined as a fracture and/or clear deformation of the femoral head matched the gross anatomical examination. The 3-D structure of the newly formed bone within the region of interest (ROI) (the central tunnel of 4 mm diameter) was reconstructed for histomorphometric analysis. Bone mineral density (BMD), bone tissue volume fraction (BV/TV), connective density (Conn. D.), trabecular number (Tb. N), trabecular thickness (Tb. Th), trabecular separation (Tb. Sp) and structure model index (SMI) in the ROIs were measured using the built-in software of HR-pQCT system.

*2.2.7. Micro finite element analysis (micro-FEA)*

Prediction of femoral fracture load was carried out by micro-FEA on the entire 40 mm reconstructed micro-CT 3-D structure of each proximal femur. To downscale the FEA calculation, eight voxels were downscaled into one voxel. A micro-FEA model of the emu proximal femur was created by converting bone voxels to brick elements [30]. Then the finite element meshes were imported into ABAQUS software (Dassault Systémes SIMULIA Inc., Vélizy-Villacoublay, France) to perform micro-FEA. The number of brick elements in the micro-finite element model ranged from 250,706 to 588,603. Bone material properties were isotropic and linear-elastic. Young's modulus was chosen as 13.05 GPa by assuming that the elastic properties of trabecular and cortical tissues were similar [31,32]. Poisson's ratio was set to 0.3 [33,34]. The distal end of each model was constrained. Load was applied vertically at the femoral head [35]. The magnitude of load was initially chosen to be 10 N for each node. Supplementary Fig. S5 showed one finite element model with boundary and loading conditions. The estimated failure load was computer based on a criterion developed by Pistoia et al. [36], in which fracture was assumed to occur when 5% of the bone tissue was strained beyond a critical limit of 7000 microstrain. In these analyses, tissue-level effective strain was calculated from the strain energy density and the Young's modulus of bone using the following equation: $\varepsilon_{eff} = \sqrt{2U/E}$. The estimated external load, which resulted in more than 5% of the bone tissue strained beyond 7000 microstrain, was taken as the predicted fracture load of the emu proximal femur.

*2.2.8. Indentation test*

Specimens without undergoing destructive evaluations were used for destructive compressive test. The proximal femur was sawed transversely at two locations, perpendicular to the long axis of the bone tunnel with a distance between the two cuts of 8 mm, so that the proximal femoral was separated into three parts (head, neck and trochanter). An indentation test was performed using an H25K-S material test machine (Hounsfield Test Equipment Ltd, Redhill, UK) on the bony part of 8 mm in thickness prepared from the mid-portion of the femoral neck. A custom-made indenter of 5 mm in diameter was used to test the mechanical properties of the healing complex with new bone formed within the bone tunnel and its integration with the adjunct residual bone. The compressive test was performed at a rate of 10 mm/min to record the maximum strength (N) and its displacement (mm) for subsequent calculation of energy (J) to failure.

*2.2.9. Histology*

The femoral head and trochanteric region were used for histology. The femoral head was bisected along the coronal plane including the trochanteric region; half of each bisected region was decalcified and embedded in paraffin while the other half was embedded in methyl methacrylate (MMA) without decalcification. Histological evaluation was performed single blindly.

*2.2.9.1. Decalcified sections.* The specimens were decalcified with 9% formic acid solution and then embedded in paraffin. The trochanter regions were sectioned transverse to the bone tunnel for hematoxylin-eosin (H&E) staining and immunohistochemistry comprising vascular endothelial growth factor (VEGF) and osteocalcin (OC). The femoral heads were sectioned along the coronal plane for fast green and safranin O staining based on published protocols [37,38]. A microscopic imaging system (Leica Q500MC; Leica Microsystems, Wetzlar, Germany) was used to digitalize the histological sections for histological observation and histomorphometric assessment using image analysis software (Image J 1.45p, NIH, USA).

Quantitation of the newly formed bone was performed by calculating the ratio of new bone within the bone channel and the entire initial bone tunnel cross sectional area using H&E stained sections. The degree of scaffold degradation in the bone tunnel was defined by evaluating the area ratio of the scaffold within entire bone tunnel at baseline (normal control group) and 12 weeks after CD surgery. The area of the bone tunnel was defined as the area in the circle around the edge of the tunnel. Formation of blood vessel and new bone within the bone tunnel was evaluated by defining the staining intensity and distribution of the VEGF and OC stained regions [39]. Polarized microscopy was used to evaluate collagen fibers alignment of the new bone formed within the implanted porous scaffolds. For articular cartilage, the maximum thickness of safranin O staining of each slide was measured as an index of cartilage matrix proteoglycans content [38].

*2.2.9.2. Undecalcified sections.* MMA embedded samples were prepared for scanning electron microscopy (SEM) (JSM-6300, JEOL, Japan) with samples sectioned at 300 μm thickness along the coronal plane using a diamond saw (Isomet, Buehler, Germany) and then polished to 200 μm using a soft cloth rotating wheel before acid-etching with 37% phosphoric acid for 20 s, followed by 5% sodium hypochlorite for 20 min [40]. The sections were then sputter-coated with gold and palladium, as described previously for SEM examination. For dynamic histology, samples were cut at 10 μm in thickness using a heavy-duty microtome (PolyCut, Leica, Germany) for Goldner's trichrome staining.

*2.3. In vitro and in vivo studies in rabbits*

*2.3.1. Primary BMSCs isolation*

Rabbit BMSCs were isolated using a standard protocol [41]. Briefly, New Zealand white rabbits (male, 20-weeks of age) were anesthetized, then bone marrow was aspirated from the iliac crests and transferred into a centrifuge tube mixed with Minimal Essential Medium - Alpha (α-MEM) (Invitrogen, Grand Island, NY, USA). Ficoll-Hypaque density media (1.077 g/ml) was added, and the mixture was centrifuged at 900 × g for 30 min for collection of mononuclear BMSCs. After washing with α-MEM twice, the cells were seeded in 75 $cm^2$ tissue culture flasks at a density $1 \times 10^6$ cells/$cm^2$ in α-MEM with 10% fetal bovine serum (FBS), 100 IU/ml penicillin and 100 μg/ml streptomycin, and placed in an incubator

at 37 °C containing 5% $CO_2$. The first medium change was done three days after cell isolation and the suspended cells were discarded. Thereafter, the medium was changed every three days. When confluence reached 80%, the cells were detached using 0.05% trypsin and passaged at the ratio of 1:3, with cells only of passage 3 being used for subsequent experiments.

*2.3.2. Effects of corticosteroid and icaritin on BMSCs differentiation*

Primary BMSCs from rabbits with or without SAON induction (SAON (+) and SAON (−)) (detailed protocol in section 2.18) were placed into 6-well plates. Firstly, the osteogenic and adipogenic differentiation potentials of BMSCs after SAON induction were examined by culturing BMSCs with α-MEM containing osteogenic supplement (OS) ($1 \times 10^{-8}$ M dexamethasone, 50 μg/ml L-ascorbic acid 2-phosphate and 10 mM glycerol 2-phosphate) or adipogenic supplement (AS) ($1 \times 10^{-6}$ M dexamethasone, 0.5 mM 3-isobutyl-1-methylxanthine, 10 μg/ml insulin and 0.2 mM indomethacin). Regarding the effects of icaritin, the osteogenic and adipogenic differentiation of BMSCs from SAON (+) and SAON (−) rabbits were studied with icaritin added, and 0.1% dimethyl sulfoxide (DMSO) served as a control. Icaritin at a range of concentrations ($10^{-8}$, $10^{-7}$, $10^{-6}$ and $10^{-5}$ M) were initially tested and $10^{-6}$ M was chosen for later studies based on the results of ALP activity. At day 10, 18 and 21 (day 3, 7 and 10 for ALP staining and assay), cells were collected for the following experiments: alkaline phosphatase (ALP) staining (BCIP/NBT kit, Novex®, Life Technologies, Grand Island, NY, USA); ALP activity assay; mineralization assay (Alizarin Red S staining); Oil Red O staining; western blot for CCAAT/enhancer-binding protein beta (C/EBP-β), peroxisome proliferator-activated receptors gamma (PPAR-γ), and adipocyte Protein 2 (aP2) for adipogenesis; and reserve transcription real-time polymerase chain reaction (RT-qPCR) for the expression of collagen, type I, alpha (COL1α), OC, runt-related transcription factor 2 (RUNX2), and bone morphogenetic protein 2 (BMP-2) for osteogenesis, and C/EBP-β, PPAR-γ, and aP2 for adipogenesis based on our published protocol [42]. After optical imaging, the Alizarin Red S stained calcium precipitates were dissolved by 10% (w/v) cetylpyridinium chloride with the absorbance read at 562 nm for quantification of the calcium formation. Triplicate tests were conducted in each experiment.

*2.3.3. Inhibition of adipogenesis with presence of composite scaffold*

Adipocyte like cell line 3T3-L1 cells were cultured in Dulbecco's Modified Eagle's Medium (DMEM) containing 10% FBS. For testing the inhibition potential of icaritin on adipocyte differentiation, cells ($10^5$/well) and composite scaffolds ($5 \times 5 \times 2$ mm$^3$, 1 piece/well) were placed simultaneously in 6-well plates overnight to reach confluence, and then the medium was changed to AS medium for 3 days before changing to adipogenic maintaining medium (DMEM containing 10 μg/ml insulin) on day 3. At day 10, the scaffolds were frozen and sectioned at a thickness of 8 μm. These sections and the cells on the bottom of the well were stained with Oil Red O [14]. A microscopic imaging system was used to digitalize the culture plates. Thereafter, the intensity of Oil Red O stained adipocytes in the well grown alongside or within the holes of the scaffold was quantified.

*2.3.4. Scratch-wound assay*

Rabbit BMSCs were cultured to confluence in 6-well tissue culture plates at a density of $1 \times 10^5$ cells/well in α-MEM medium and then starved overnight. The confluent cell monolayer was then scraped with a tip [43] and incubated for 12 h with the serum free medium containing $10^{-6}$ M icaritin or 0.1% DMSO control. BMSCs migration was quantified microscopically at time points of 0, 6, and 12 h. The wound widths were measured using Image-Pro Plus (Media Cybernetics, Rockville, MD, USA). The mRNA expression of vascular cell adhesion molecule 1 (VCAM1), stromal cell-derived factor 1 (SDF1) and chemokine receptor type 4 (CXCR4) was examined by RT-qPCR.

*2.3.5. BMSCs recruitment*

P/T and P/T/I scaffolds of $0.5 \times 0.5 \times 0.25$ cm$^3$ were prepared for sterilization by 70% alcohol before UV treatment for 30 min. Six scaffolds were placed and fixed to the bottom of each well of a 6-well plate (Fig. 16A). A total of $5 \times 10^4$ BMSCs were placed into each well and cultured for 24 h before counting the cell density, i.e. number of BMSCs per unit area (cm$^2$/cells) around the scaffold within a defined area of $2.5 \times 5$ mm$^2$ away from the scaffold (Fig.16C). The mRNA expression of VCAM1 in BMSCs was evaluated by RT-qPCR.

*2.3.6. RT-qPCR and western blot*

RNA was isolated from the treated BMSCs using RNeasy® Mini Kit and reverse transcribed into cDNA by QuantiTect® Reverse Transcription Kit (Qiagen, Hilden, Germany). cDNA was used as template for RT-qPCR. Primer sequences of rabbit genes of interest, COL1α, OC, RUNX2, BMP-2, C/EBP-β, PPAR-γ, aP2, VCAM1, SDF1, CXCR4 and glyceraldehyde 3-phosphate dehydrogenase (GAPDH) as the housekeeping gene were listed in the Supplementary Table S1. RT-qPCR was performed in 384-well plates using TF pack Power SYBR Green PCR Master Mix and ABI Prism 7700 sequence Detection System (Applied Biosystem, Foster City, CA, USA).

Proteins from BMSCs cultured in adipogenic induction medium with or without icaritin were extracted by NE-PER nuclear and cytoplasmic extraction reagents kit (Cat# 78833, Pierce, Rockford, IL, USA). The concentration of protein was measured by BCA protein assay kit (Cat# 23225, Pierce). Fifty micrograms of protein was separated by 10% SDS-PAGE and transferred to PVDF membrane by buffer-tank–blotting apparatus (Bio-Rad, Hercules, CA, USA). After blocking with 5% fat-free milk for 1 h, the membrane was incubated with primary antibody PPAR-γ, aP2 and β-actin (Santa Cruz Biotechnology, Dallas, TX, USA) overnight at 4 °C, then incubated with secondary antibody conjugated to horseradish peroxidase (Santa Cruz Biotechnology) for 1 h. After washing with tris-buffered saline and tris-buffered saline Tween-20, the protein was detected and visualized by Amersham ECL Plus™ Western Blotting Detection (GE Healthcare, Little Chalfont, UK).

*2.3.7. Superparamagnetic iron oxide (SPIO) labeling*

SPIO labeling was performed on rabbit BMSCs reaching 80% confluence. SPIO nanoparticles (5 μg/ml) were coated with silica and functionalized with amines (SPIO@$SiO_2$–$NH_2$), suspended in serum free α-MEM, and then sonicated for 30 min at 100 V for dispersing the aggregated particles. Details about SPIO preparation and cell labeling were published previously [44,45]. BMSCs were washed by phosphate buffered saline to remove the serum thoroughly prior incubation with SPIO for 16 h. The labeled BMSCs were then used for the following *in vivo* mechanistic study in rabbits visualized using Prussian blue staining based on our published protocol [44].

*2.3.8. Rabbit SAON model*

Twelve 22-week-old male New Zealand white rabbits with body weight of 3.5–4 kg were used with experimental protocols approved by Animal Experiment Ethics Committee of the Chinese University of Hong Kong (09/003/GRF). SAON was induced with LPS and MPS in these rabbits based on our published protocol [46]. Two weeks post-induction, CD was performed under general anesthesia with xylazine (20 mg/kg body weight) and ketamine (50 mg/kg body weight). A bone tunnel of 3.0 mm in diameter was drilled by a

trephine through the distal femur, from the attachment of the medial collateral ligament to the contralateral cortex, parallel to the coronal plane of the knee joint (Fig. 3A). The P/T (n = 6) and P/T/I (n = 6) scaffolds were randomly implanted into left or right distal femur (Fig. 3B). In order to find out whether P/T or P/T/I scaffold would attract mesenchymal stem cells (MSCs), SPIO pre-labeled BMSCs were injected into the bone marrow. A total of 500 μl suspension of pre-labeled BMSCs ($1 \times 10^7$ cells) was injected into the bone marrow 20 mm proximal to the implantation site for histological analysis (Fig. 3C).

#### 2.3.9. Histology and histomorphometry

One week after scaffold implantation, the rabbits were euthanized for sample harvesting. The tunnel region was selected for analysis. The femora were collected and fixed with buffered formalin and decalcified by 9% formic acid solution. After decalcification, the specimens were dehydrated and embedded in paraffin for sagittal sectioning at 6 μm in thickness using a microtome, stained with Prussian blue and then counterstained with nuclear fast red using standard protocols [47].

### 2.4. Statistical analysis

All numeric data were expressed as mean ± SD. The incidence of collapse in emu model was defined as the number of collapsed hips divided by the total number of hips in each group, and analyzed with Fisher's exact probability test. One-way analysis of variance (ANOVA) followed by Tukey's post-hoc test (multi-group comparison) and unpaired-sample *t*-test (two-group comparison) were used to assess statistical significance set $p < 0.05$. Statistical analysis was performed using SPSS 17.0 software (IBM, Armonk, NY, USA).

## 3. Results

### 3.1. Emu efficacy study

#### 3.1.1. Gait analysis and MRI imaging

Cripple gait pattern during loading and unloading gait cycle was not observed until week 12 in some emus after SAON induction. One week after CD surgery, emus with scaffold implantation recovered with a normal gait while an abnormal gait was still found in empty control group emus (Supplementary Video S2 and S3).

Supplementary video related to this article can be found at http://dx.doi.org/10.1016/j.biomaterials.2015.04.038.

On T2-weighed MR imaging, a subchondral osteonecrosis in the proximal femur was found at 12 weeks following pulsed induction with LPS and MPS (Fig. 4A). One week after CD surgery, MR imaging confirmed a satisfactory tunneling procedure with the tunnel extending from the lateral femoral cortex to the subchondral bone (Fig. 4B).

#### 3.1.2. Incidence of hip collapse

No emus died of surgery or over the entire follow-up period of 24 weeks. The external appearance of the femoral head was imaged by digital photography while the cross sectional image of the bone tunnel at the endpoint was imaged by micro-CT (Fig. 5). Femoral head collapse incidence was 70% in empty control group, 30% in P/T group and only 10% in P/T/I group. Fisher's exact probability test showed that the collapse incidence in the P/T/I group was significantly lower than the empty control group ($p < 0.01$).

#### 3.1.3. Articular cartilage of femoral head

The articular cartilage thicknesses at both collapsed region and intact region were 76% and 51% higher in P/T/I group than in empty control group, respectively ($p < 0.05$ for both). Although there was no statistically significant difference between P/T group and empty control group, or between P/T group and P/T/I group, the average cartilage thickness in P/T/I group was still larger (24% at the collapsed region and 26% at the intact region) than that of P/T group, and P/T group was also thicker (43% at the collapsed region and 20% at the intact region) than that of empty control group (Table 1).

The cartilage stiffness at both tested regions of both P/T/I group and P/T group were significantly higher (130% at the collapsed region and 119% at the intact region for P/T/I group, 74% at collapsed region and 73% at intact region for P/T group) than those in empty control group, respectively ($p < 0.01$) (Table 1). The average cartilage stiffness at both tested regions was higher in P/T/I group than those in P/T group, yet without reaching statistical significance.

The representative safranin O and fast green stained images and thickness measurement were shown in Fig. 6. The maximum thickness of safranin O stained tissue among groups were statistically different ($p < 0.5$) with a maximum of 2.5 mm in thickness found in P/T/I group (Table 1).

#### 3.1.4. Micro-CT analysis of bone tunnel

Quantitative micro-CT analysis was performed for evaluating new bone formation and its microarchitecture within the bone tunnel in emu proximal femur (Fig. 7). Implantation with either P/T or P/T/I scaffold enhanced new bone formation in the bone tunnel

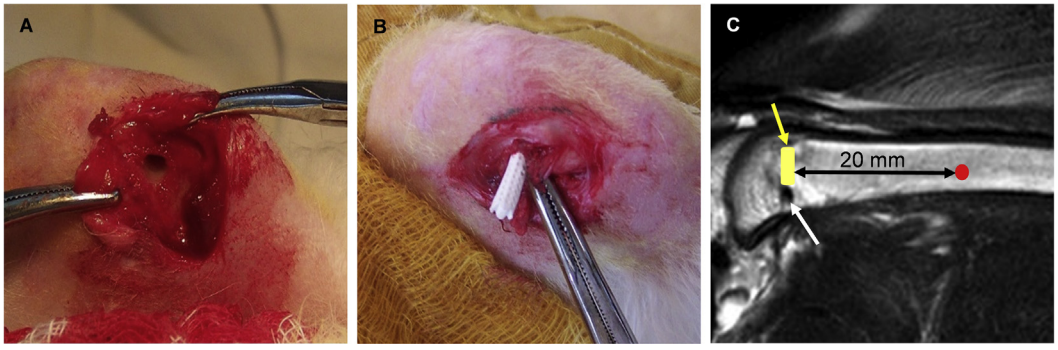


**Fig. 3.** Implantation of cylindrical scaffold and site of SPIO labeled BMSCs injection of the SAON rabbit model. (A) A bone tunnel (indicated by white arrow) was created by 3.0 mm trephine at the coronal plane of the distal femur that simulated CD in SAON rabbit. (B) The cylindrical scaffold was implanted into the bone tunnel of the distal femur. (C) Total of 500 μl ($10^7$ cells) SPIO labeled MSCs suspension was injected into bone marrow cavity at the midshaft of femur with a distance of 20 mm away from the implanted scaffold (red dot: SPIO injection site; yellow arrow: the implanted scaffold; white arrow: bone tunnel). (For interpretation of the references to color in this figure legend, the reader is referred to the web version of this article.)

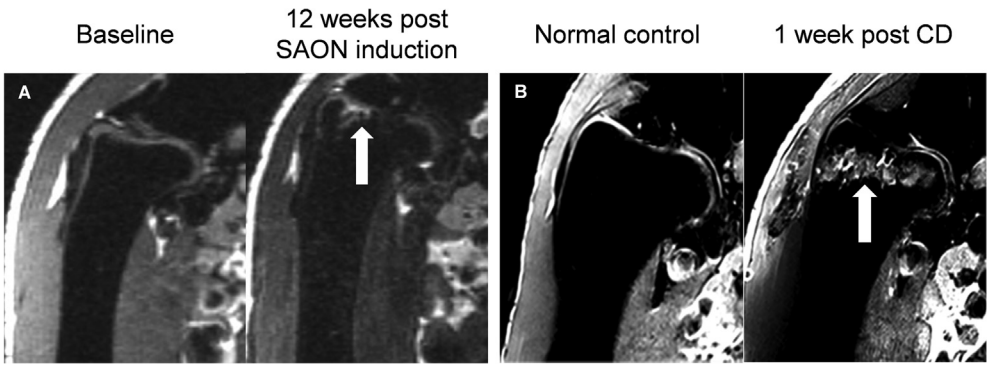


**Fig. 4.** T2 weighed MRI showing SAON development and scaffold implantation. (A) Subchondral abnormal high signal (white arrow) in the right proximal femur was found 12 weeks after SAON induction. (B) MRI images of (left) normal control with intact hip and (right) a bone tunnel (white arrow) beginning from the lateral femoral cortex to the subchondral bone created by CD with scaffold implantation.

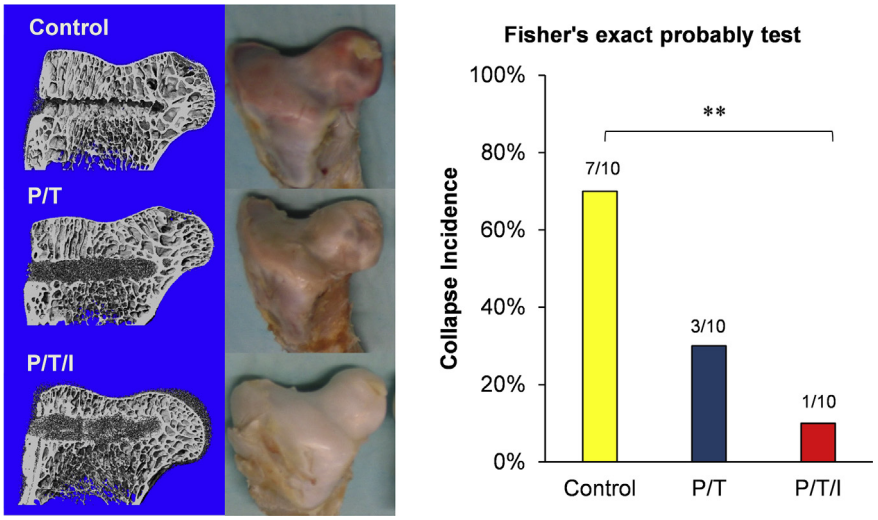


**Fig. 5.** Incidence of joint collapse. Left & middle: Coronal cross sectional micro-CT images and digital photos of emu femoral head 12 weeks after surgical core decompression. Right: Incidence of femoral head collapse analyzed by Fisher's exact probability test. **: $p < 0.01$ ($n = 10$) for group difference.

while no bone was observed in empty control. Bone tunnel with P/T/I scaffold showed more bone formation when compared to P/T scaffold. Significant higher BMD ($mg/cm^3$) ($p < 0.01$), BV/TV ($p < 0.05$), Conn.D ($mm^{-3}$) ($p < 0.05$), Tb.N ($mm^{-1}$) ($p < 0.01$) and Tb.Th (mm) ($p < 0.05$) but lower Tb.Sp (mm) ($p < 0.01$) and SMI ($p < 0.05$) were found in P/T/I group as compared with that of P/T group (Table 2).

### 3.1.5. Fracture load by micro-FEA

The estimated fracture load of emu proximal femur was provided by micro-FEA (Supplementary Fig. S6). Results showed that the failure loads were statistically significantly different among the three groups ($p < 0.05$), with the highest (7408 ± 2200 N) in P/T/I group, followed by P/T group (5824 ± 935 N), and empty control group (4521 ± 467 N) (Table 3).

**Table 1**
Cartilage thickness and stiffness measured by ultrasound indentation 12 weeks after core-decompression surgery with or without scaffold implantation.

| | Empty control (n = 10) | P/T (n = 10) | P/T/I (n = 10) |
|---|---|---|---|
| **Collapsed region** | | | |
| Thickness (mm) | 0.4 ± 0.2 | 0.6 ± 0.4 | 0.7 ± 0.4* |
| Stiffness (kPa) | 3.03 ± 1.33 | 5.28 ± 2.98** | 6.98 ± 3.67** |
| **Intact region** | | | |
| Thickness (mm) | 0.9 ± 0.3 | 1.1 ± 0.3 | 1.4 ± 0.4* |
| Stiffness (kPa) | 5.28 ± 1.93 | 9.12 ± 3.50** | 11.54 ± 4.40** |

*: $p < 0.05$ and **: $p < 0.01$, compared with the control.

### 3.1.6. Mechanical properties

The indentation test showed that the maximum strength and energy to failure in P/T/I group and P/T group were both significantly higher than those in empty control group ($p < 0.05$). Both parameters in P/T/I group were also significantly higher (78.8% for maximum strength and 87.2% for energy) than that of P/T group ($p < 0.05$) (Table 3).

### 3.1.7. Histology, immunohistochemistry and SEM

The histomorphological evaluation of bone healing in the tunnel is shown in Fig. 8. There was almost no new bone formed in empty control group (Fig. 8A1&B1). The bone tunnel was filled with more new trabecular bone in P/T/I group (Fig. 8A3&B3) while less new bone was observed in P/T group (Fig. 8A2&B2). The area ratio of newly formed bone in P/T/I group was significantly larger than that in P/T group ($p < 0.05$, Table 4). The difference in the degradation ratio of both types of scaffolds was not statistically significant with a slightly higher rate in P/T/I group (Table 4). Under polarized microscope, there were more parallel collagen fibers in the newly formed bone in P/T/I group than that in P/T group (Fig. 8C1–3).

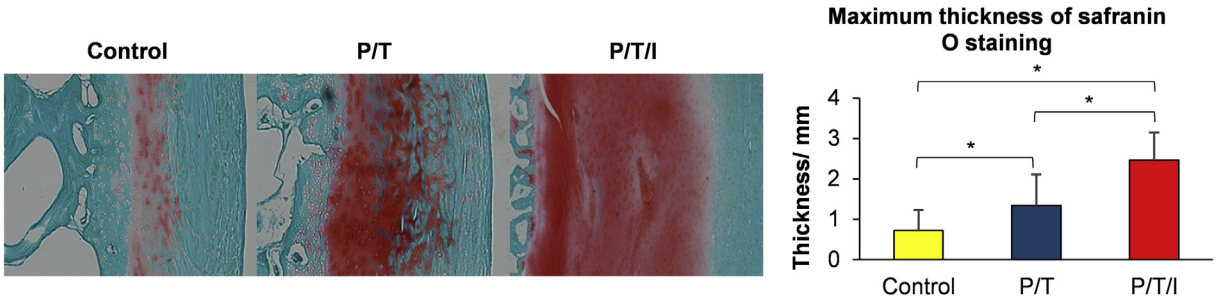


**Fig. 6.** Cartilage matrix proteoglycan content expression. Left: Histological sections of emu femoral head articular cartilage stained by safranin O and fast green of the control, P/T and P/T/I groups. Right: The maximum thickness of safranin O stained region was measured and plotted. Statistical differences in the maximum thickness of safranin O stained cartilage among three groups (*: $p < 0.05$, $n = 10$).

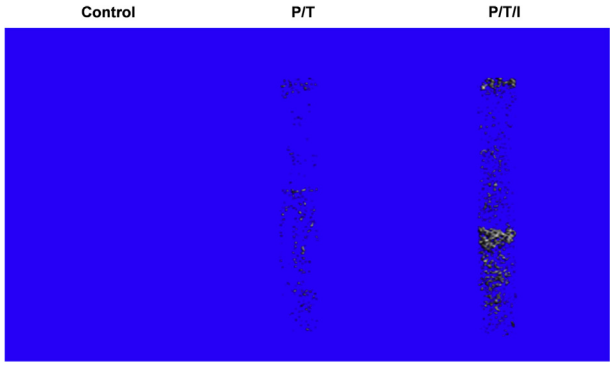


**Fig. 7.** Representative 3-D micro-CT images of the bone tunnel after core-decompression (CD). Formation of new bone within a ROI of central 4 mm of the entire bone tunnel of emu femur 12 weeks after CD and scaffold implantation.

**Table 2**
Quantitative analysis of micro-CT for the newly formed bone within bone tunnel 12 weeks after core-decompression surgery with or without scaffold implantation.

| | Empty control (n = 10) | P/T (n = 10) | P/T/I (n = 10) |
|---|---|---|---|
| BMD (mg/cm$^3$) | 0.05 ± 0.07 | 11.94 ± 5.81** | 29.15 ± 11.77**## |
| BV/TV (%) | 0.04 ± 0.07 | 1.04 ± 0.51** | 2.95 ± 2.39**# |
| Conn.D (mm$^{-3}$) | N/A | 0.08 ± 0.04 | 0.18 ± 0.12# |
| Tb.N (mm$^{-1}$) | N/A | 0.73 ± 0.07 | 0.91 ± 0.13## |
| Tb.Th (mm) | N/A | 0.13 ± 0.03 | 0.17 ± 0.06# |
| Tb.Sp (mm) | N/A | 1.40 ± 0.15 | 1.13 ± 0.15## |
| SMI | N/A | 4.83 ± 0.24 | 4.66 ± 0.18# |

**: $p < 0.01$, compared with the control; #: $p < 0.05$ and ##: $p < 0.01$, compared with P/T group.

The immunohistochemical staining of OC and VEGF are shown in Fig. 8D&E. There were scattered OC signals shown in empty control group while more signals were observed in P/T group. Most signals in P/T group were present around the edge of the bone tunnel. Less OC signals were found in P/T/I group compared to P/T group; the signals in P/T/I group were mainly found at the edge of newly formed bone. Scattered VEGF signals were observed in empty control group. In P/T group, the signal spread mainly on or next to the edge of the bone tunnel with clusters of staining signals found near the edge of tunnel where some bone-like tissue was present. Less VEGF signal was observed in P/T/I group than that of P/T group.

Goldner's trichrome staining for osteoid of the new bone within the bone tunnel is shown in Fig. 9. There was less new active bone formation found in P/T group while more new bone with osteoid and mineralized bone matrix were observed in P/T/I group.

SEM images showed that there was no osteocyte-like structure at the subchondral bone of the collapsed region in empty control (Fig. 10A) while there were some osteon-like structures in normal control group (Fig. 10B). The micro-structures of trabecular bone at the border of bone tunnel in P/T (Fig. 10C) and P/T/I groups (Fig. 10D) were similar to that of normal control group.

### 3.2. Mechanistic study using convenient rabbit model

#### 3.2.1. Differentiation potential of BMSCs from SAON rabbits

Two weeks after SAON induction, BMSCs were isolated from SAON (+) rabbits and SAON (−) normal rabbits for comparison: 1) Compared with SAON (−) group, the quantitative ALP activity of BMSCs decreased significantly by 69%, 64% and 67% in SAON (+) groups when osteogenic induction was performed and evaluated continuously at day 3, 7 and 10, respectively (Fig. 11A). ALP expression of BMSCs also decreased in SAON (+) group at day 3, 7 and 10 (Fig. 11B). 2) Calcium deposition by SAON (+) group at all time points was observed to have significantly less calcium nodule formation as compared with SAON (−) group (Fig. 11C). 3) After adipogenic induction for 21 days, both the number and size of the adipocytes increased in SAON (+) group as compared to that of SAON (−) group (Fig. 11D). These findings demonstrated that BMSCs of SAON (+) group had a significantly impaired differentiation potential in osteogenesis accompanied with elevation of adipogenic ability.

#### 3.2.2. Effects of icaritin on differentiation of BMSCs

Icaritin was added to the culture medium to investigate its

**Table 3**
Mechanical properties of emu femoral head 12 weeks after core-decompression surgery with or without scaffold implantation.

| | Empty control (n = 10) | P/T (n = 10) | P/T/I (n = 10) |
|---|---|---|---|
| **FEA**[a] | | | |
| Predicted fracture load (N) | 4521 ± 467 | 5824 ± 935* | 7408 ± 2200*# |
| **Indentation test**[b] | | | |
| Maximum Strength (N) | 11.16 ± 12.40 | 26.31 ± 19.82* | 47.03 ± 33.58*# |
| Energy (J) | 0.0052 ± 0.00284 | 0.0094 ± 0.0042* | 0.0176 ± 0.0047*# |

a: fracture load of entire femoral head was predicted by FEA; b: tested for compressive properties of the middle 8 mm section of emu femoral head. *: $p < 0.05$, compared with the control; #: $p < 0.05$, compared with P/T group.

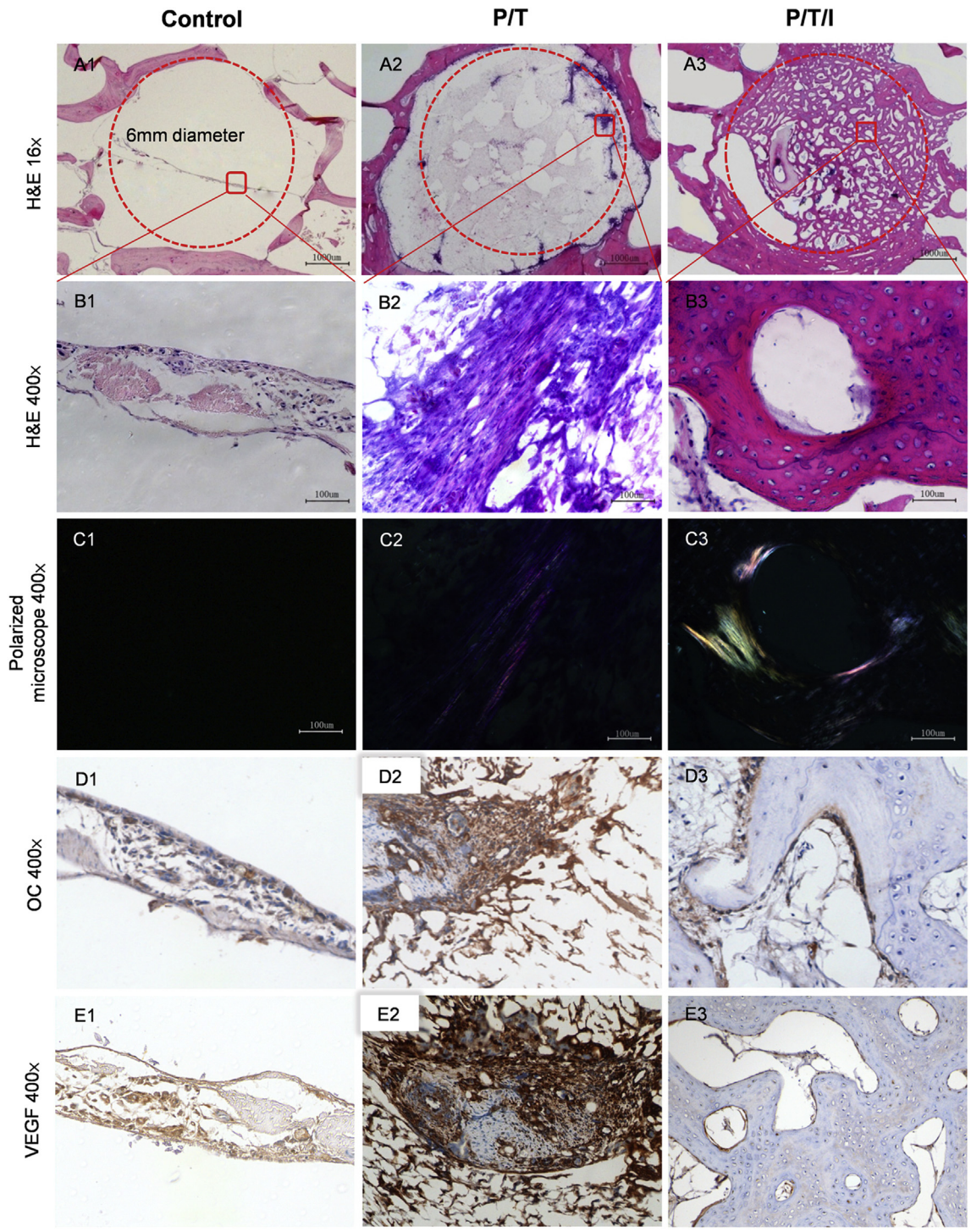


**Fig. 8.** Representative histological images of bone tunnel in emu proximal femur. (A&B) H&E staining of the bone tunnel at magnifications of 16× and 40×. (C) Microphotograph of the bone section under polarized light at a magnification of 400× for collagen observation. Immunohistochemical staining of (D) OC and (E) VEGF expressed on bone section within the bone tunnel with positive cells stained brown at magnifications of 400×. (For interpretation of the references to color in this figure legend, the reader is referred to the web version of this article.)

effects on the osteogenesis and adipogenesis of BMSCs from SAON (+) and SAON (−) rabbits for the following findings: 1) ALP activity assay showed that icaritin enhanced ALP activity in a dose-dependent manner in both SAON (−) and SAON (+) groups, with an optimal icaritin concentration of $10^{-6}$ M. ALP activity at day 10 was enhanced by 70% and 179% in SAON (−) and SAON (+) groups respectively (Fig. 12A). Icaritin elevated ALP expression both in SAON (−) and SAON (+) groups with more obvious staining intensity change in SAON (+) group (Fig. 12B). 2) Icaritin increased calcium deposition in both SAON (−) and SAON (+) groups (Fig. 12C). Quantification of calcium nodules showed that the addition of icaritin increased the formation of calcium nodules by 43% and 71% in SAON (−) and SAON (+) groups, respectively (Fig. 12D). 3) RT-qPCR showed that COL1α, OC, RUNX2 and BMP-2

**Table 4**
Histomorphometric analysis of areal fraction of new bone and scaffold within the bone tunnel 12 weeks after core-decompression surgery with or without scaffold implantation.

| | Empty control (n = 10) | P/T (n = 10) | P/T/I (n = 10) |
|---|---|---|---|
| Area fraction of newly formed bone (%) | 0.1480 ± 0.2563 | 3.924 ± 1.50* | 14.38 ± 21.08*# |
| **Area fraction of scaffold (%)** | | | |
| At baseline | N/A | 47.24 ± 4.43 | 54.00 ± 6.31 |
| At week 12 after implantation | N/A | 32.30 ± 12.42 | 24.06 ± 17.47 |

N/A: not applicable; *: $p < 0.05$, compared with the control; #: $p < 0.05$, compared with P/T group.

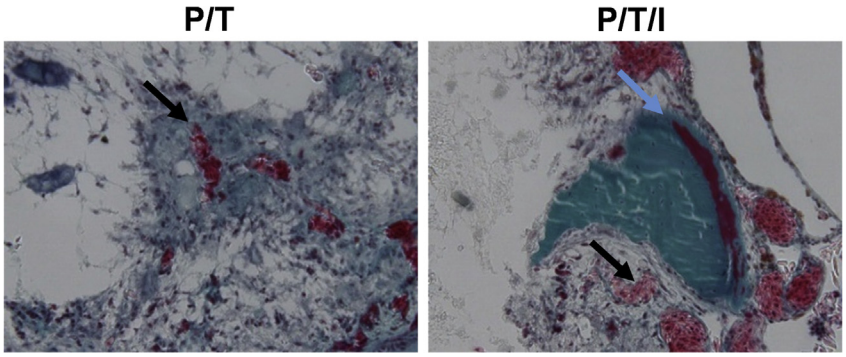


**Fig. 9.** Goldner's trichrome staining of the bone-like tissue within the bone tunnel. Histological sections of the P/T and P/T/I groups showing little newly formed bone (black arrow) with no observable osteoid in P/T group and more new bone formation (black arrow) with osteoids (blue arrow) and mineralized bone matrix (stained green) in P/T/I group. (For interpretation of the references to color in this figure legend, the reader is referred to the web version of this article.)

expression of SAON (+) group decreased about 4.5-fold, 3-fold, 9-fold and 4-fold compared to SAON (−) group. Icaritin significantly increased COL1α, OC, RUNX2 and BMP-2 expression 7.5-fold, 5-fold, 13.5-fold and 6.5-fold in SAON (−) group and 10-fold, 3-fold, 14-fold and 5-fold in SAON (+) group (Fig. 12E). 4) Lipid droplets were significantly increased by 57% in SAON (+) group compared to SAON (−) group ($p < 0.01$); with icaritin treatment, lipid deposition decreased by 44% and 37% in SAON (−) and SAON (+) groups, respectively (Fig. 12F&G) ($p < 0.01$ for both). The expression of adipogenic differentiation regulatory genes C/EBP-β, PPAR-γ and aP2 in SAON (+) group was higher than SAON (−) group by 15, 10 and 8 times ($p < 0.01$); while these two groups were treated with icaritin, the C/EBP, PPAR-γ and aP2 expression was reduced by 77%, 67%, and 55% in SAON (−) group ($p < 0.01$) and 72%, 67% and 73% in

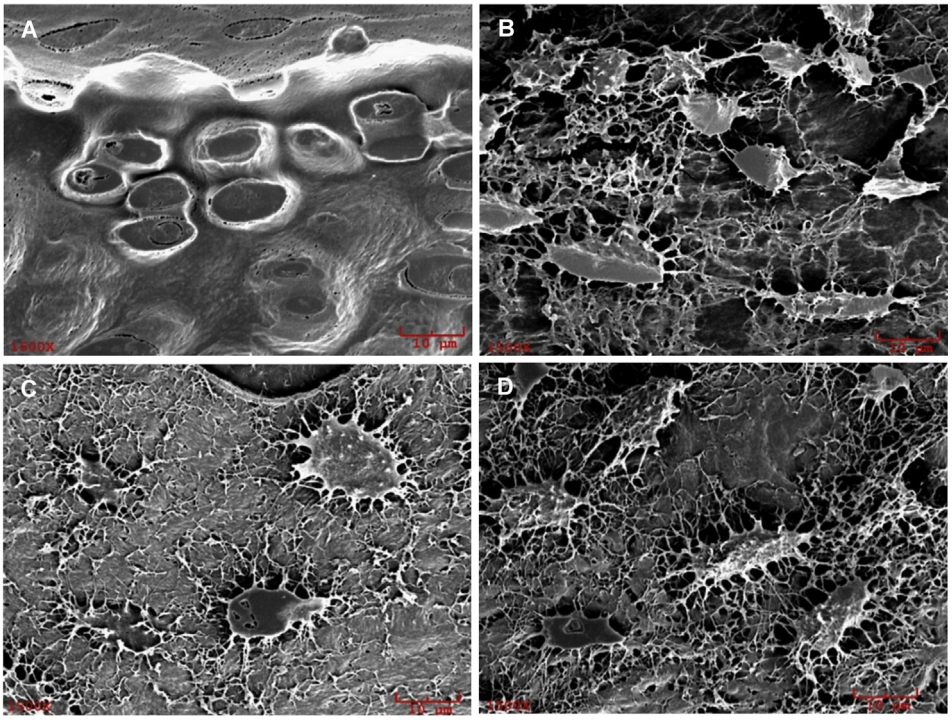


**Fig. 10.** Representative SEM images of the bone from emu femoral head (1500×). SEM images from (A) subchondral bone of the collapsed region of the empty control, (B) subchondral bone of the normal control with SAON induction, (C) trabecular bone at the border of bone tunnel in P/T group, and (D) trabecular bone at the border of bone tunnel in P/T/I group.

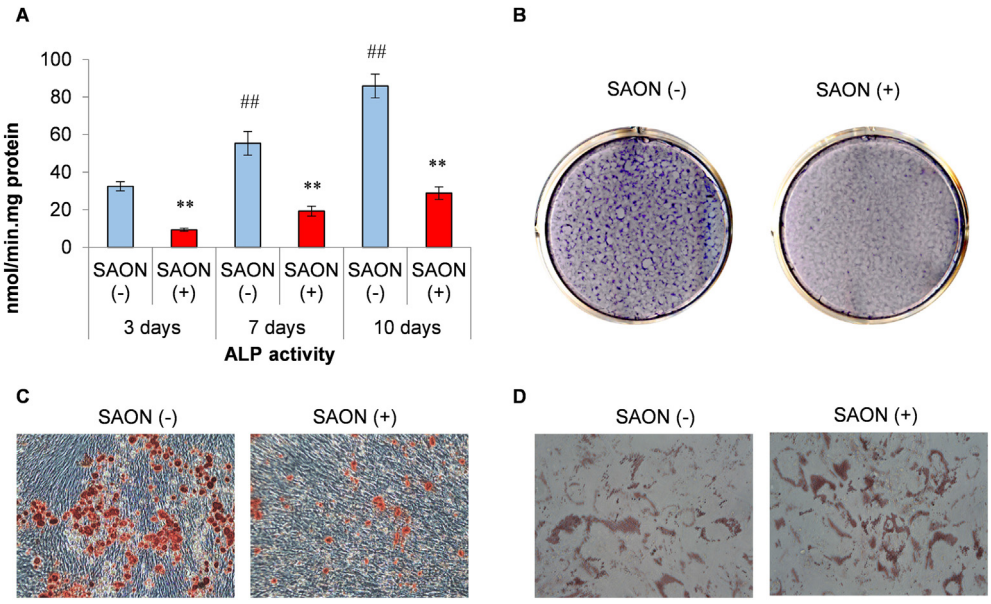


**Fig. 11.** Differentiation potential of BMSCs derived from normal and SAON rabbits. (A) ALP activity assay were measured on day 3, 7 and 10 days after BMSCs cultured in OS medium (mean ± SD, n = 3); **: $p < 0.01$ among groups; ##: $p < 0.01$ vs. all other groups. (B) ALP staining of BMSCs treated with OS medium for 10 days. (C) Calcium nodule staining of BMSCs treated with OS medium for 18 days (Alizarin Red S, 10×). (D) Lipid droplet formation of BMSCs treated in AS differentiation medium for 21 days (Oil Red O staining, 20×).

SAON (+) group ($p < 0.01$) (Fig. 12H). Accordingly, the change in protein level expression of PPAR- γ and aP2 was also examined. Western blot results showed that PPAR- γ and aP2 expression was upregulated in SAON (+) group, while the expression of PPAR- γ and aP2 proteins of SAON (−) and SAON (+) groups was obviously lower after the addition of icaritin (Fig. 12I).

### 3.2.3. Adipogenesis of 3T3-L1 cells on scaffold

The effect of P/T/I scaffold on adipogenesis of 3T3-L1 was determined by Oil Red O staining. Lipid droplet formation (Fig. 13A) next to the scaffold in P/T group was slightly inhibited when compared to control group, where BMSCs were seeded onto the standard tissue culture flask. For P/T/I scaffold, lipid droplet formation either next to the scaffold or within the hole of the scaffold was greatly inhibited when compared to that of P/T group. Quantification of Oil Red O staining for the lipid droplet formation next to the scaffold showed a significant decrease ($p < 0.01$) in P/T/I group when compared to P/T or control group (Fig. 13B). Comparing Oil Red O stained adipocytes within the drilled hole, it was found that the stained area of P/T/I scaffold was significantly less ($p < 0.01$) than that of P/T scaffold (Fig. 13C).

### 3.2.4. Effects of icaritin on migration of BMSCs

Scratch wound healing assay was carried out to determine the effect of icaritin on the migration of SAON (−) normal BMSCs. BMSCs exposed to icaritin containing medium migrated into the denuded area and recovered the exposed surface within a shorter time period than BMSCs exposed to DMSO containing control medium (Fig. 14A). Quantification of the cell migration rate showed that the migration rate of BMSCs cultured in medium with icaritin was significantly increased by 31% than that of control group ($p < 0.05$) (Fig. 14B). The expression of migration factors by BMSCs was detected using RT-qPCR after treatment with icaritin for 24 h. CXCR4/SDF1 genes expression did not have any obvious difference while migration regulatory gene VCAM1 expression increased significantly ($p < 0.01$) with icaritin treatment (Fig. 15).

### 3.2.5. Effects of scaffold on BMSCs recruitment

As icaritin alone could promote migration of BMSCs as confirmed above, we further tested the ability of P/T or P/T/I scaffold for potential recruitment of BMSCs *in vitro* (Fig. 16). BMSCs grown away from (Fig. 16B1&3) and near to (Fig. 16B2&4) the scaffolds were imaged by optical microscope for quantification. There were 110% and 274% more cells around P/T and P/T/I scaffolds than other regions distant from the scaffolds of the corresponding wells (Fig. 16D). P/T/I group attracted 70% more BMSCs than that of P/T group ($p < 0.05$). mRNA expression of migration gene VCAM1 was measured using RT-qPCR in order to detect at which stage that the scaffolds impacted migration of BMSCs. The mRNA expression of VCAM1 increased by 61% in P/T/I group while there was no changes found in P/T group as compared to control group (Fig. 16E).

### 3.2.6. Scaffold on homing of BMSCs in vivo.

SAON rabbit model with SPIO labeled BMSCs was chosen for studying the role of P/T and P/T/I scaffolds on the recruitment of stem cells for bone healing and preventing subsequent hip joint collapse caused by SAON. Presence of SPIO labeled BMSCs in the histological section could be observed by Prussian blue staining (Fig. 17A). It was found that without scaffold implantation, the tunnel was filled dominantly with fat cells, and there was no observable labeled BMSC in the tunnel. On the other hand, SPIO positive BMSCs, which were injected 20 mm away from the bone tunnel, were clearly observed to migrate and spread evenly into both P/T and P/T/I scaffolds implanted in the tunnels. There was no statistically significant difference in the number of SPIO labeled cells in the tunnel regions between P/T and P/T/I groups (Fig. 17B).

## 4. Discussion

This is the first study to demonstrate that P/T/I, a phytomolecule-based bioactive composite scaffold, can be an effective bone filler for prevention of hip joint collapse using our recently established bipedal SAON emu model [23], while the underlying mechanism has been studied *in vitro* using rabbit BMSCs [9] and *in vivo* with a well-established cost-effective and easy-

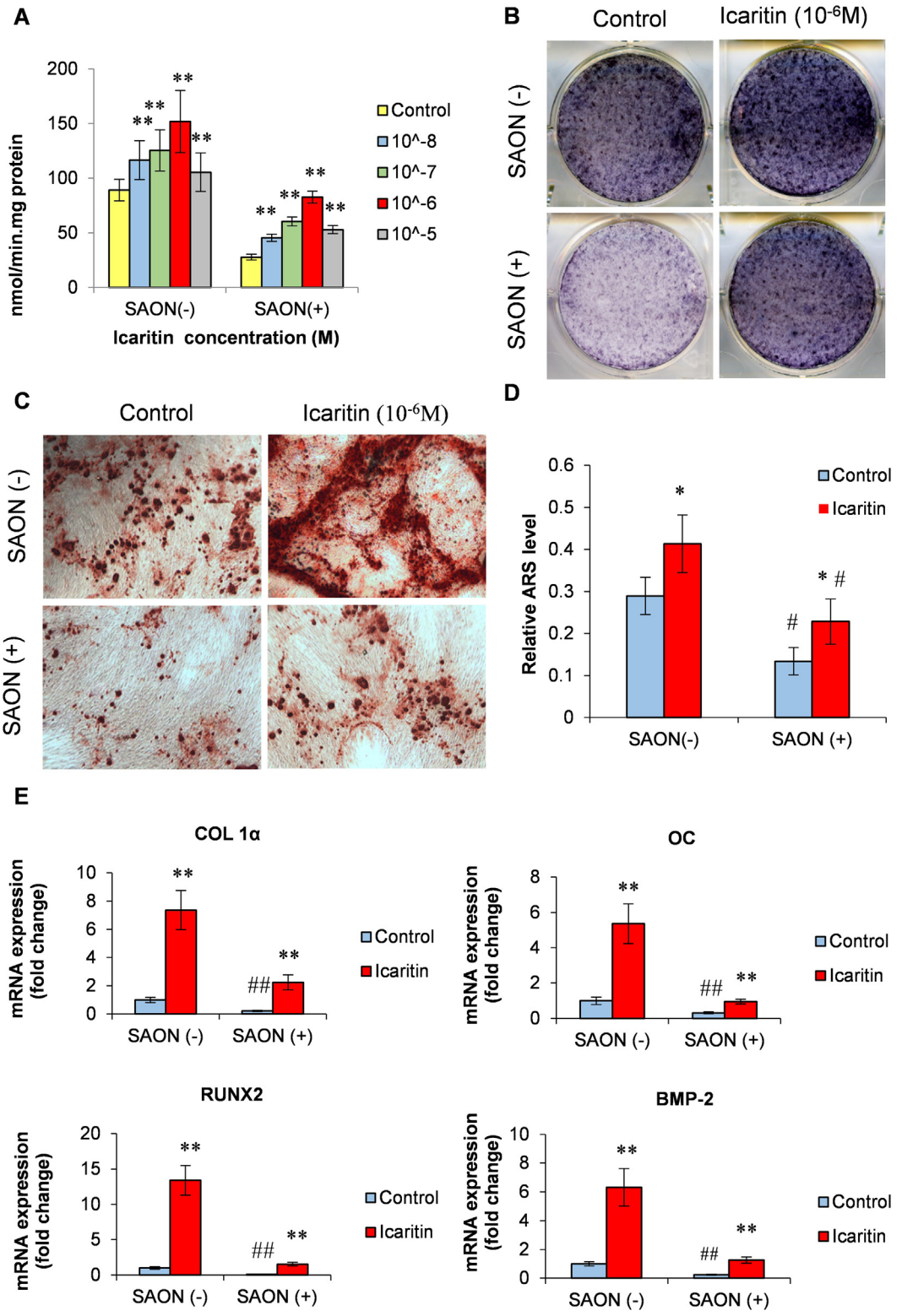


**Fig. 12.** Icaritin on osteogenic and adipogenic differentiation of BMSCs derived from normal and SAON rabbits (n = 3). (A) ALP activity of BMSCs treated with icaritin ($10^{-8}$ M to $10^{-5}$ M) in OS medium for 10 days. (B) ALP staining of BMSCs treated with $10^{-6}$ M icaritin in OS medium for 10 days. (C) Calcium nodule formation of BMSCs treated with or without icaritin in OS medium for 18 days (Alizarin Red S, 10×). (D) Relative Alizarin Red S (ARS) staining intensity quantified for calcium nodule formation in (C) determined by absorbance measurement at 562 nm. (E) mRNA expression (RT-qPCR) of COL1α, OC, RUNX2 and BMP-2 of BMSCs cultured in OS medium with or without icaritin for 10 days. (F) Oil Red O staining intensity of BMSCs cultured in AS differentiation medium with or without icaritin for 21 days. (G) Quantification of Oil Red O in (F) at 520 nm OD. (H) mRNA level of adipogenic genes C/EBP-β, PPAR-γ and aP2 after adipogenic induction for 21 days with or without icaritin treatment. (I) PPAR-γ and aP2 expression of BMSCs cultured in adipogenic induction medium for 21 days with or without icaritin treatment (western blot, β-actin served as the loading control). *:$p < 0.05$ and **:$p < 0.01$, icaritin vs. control; #: $p < 0.05$ and ##: $p < 0.01$, SAON (+) vs. SAON (−).

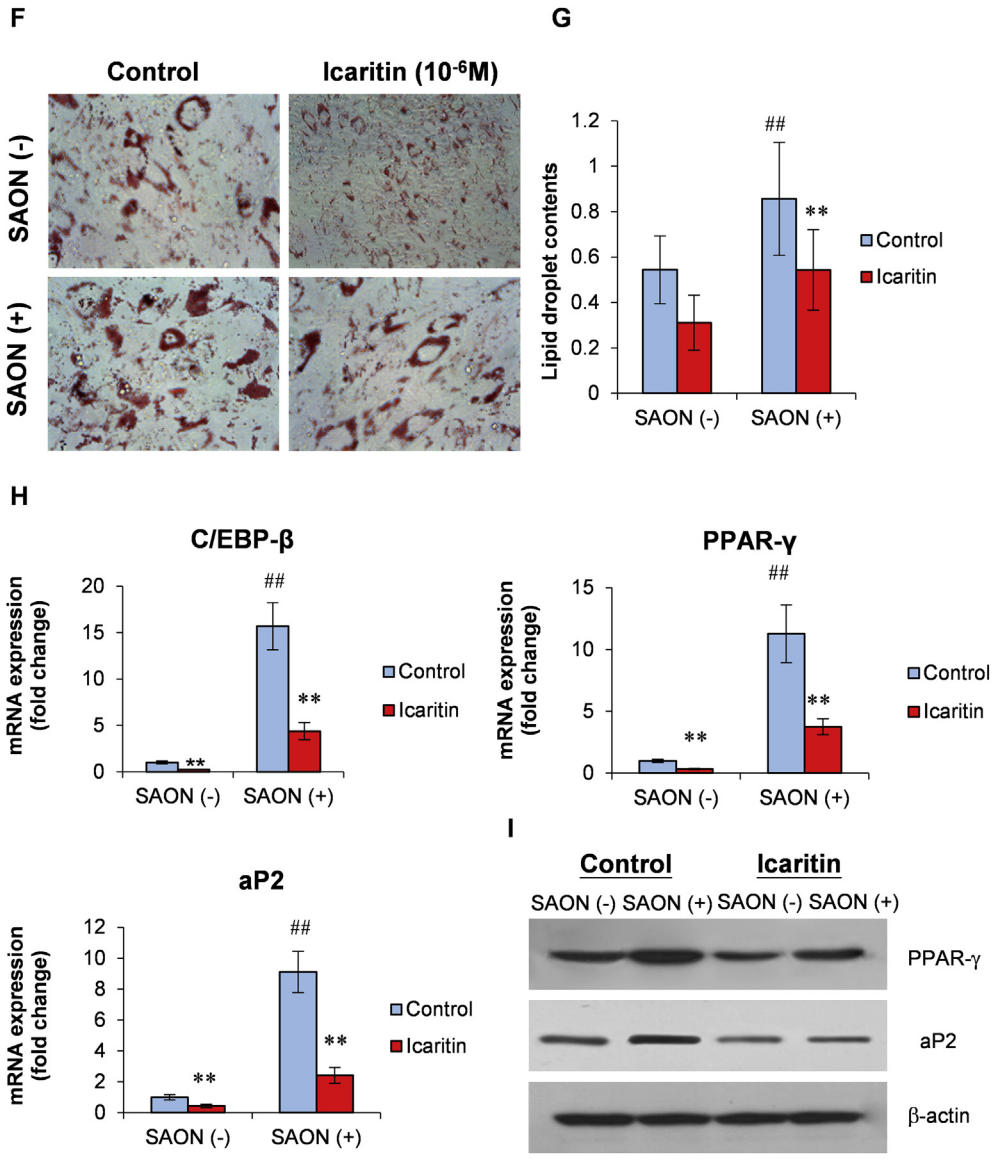


**Fig. 12.** (*continued*).

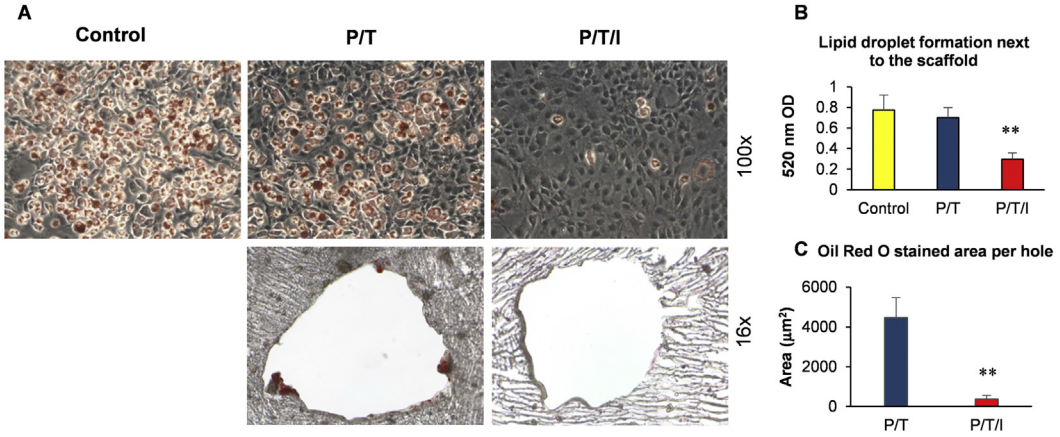


**Fig. 13.** Adipogenesis of 3T3-L1on 3-D P/T and P/T/I scaffolds. (A) Oil Red O staining of the control (standard tissue culture treated surface), P/T and P/T/I groups shows the lipid formation next to (upper row, 100×) and within the holes (lower row, 16×) of the scaffolds. Quantification of Oil Red O staining for lipid droplet formation (B) next to and (C) within the holes of the scaffolds. **: $p < 0.01$ P/T/I group compared to the control or P/T scaffold.

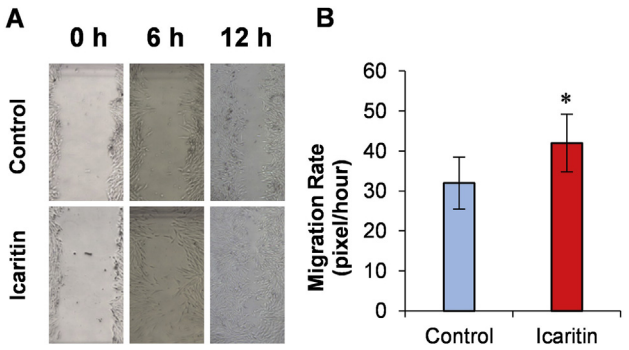


**Fig. 14.** Icaritin on *in vitro* scratch wound healing assay of BMSCs. (A) Tissue culture plates grown with rabbit BMSCs monolayer were scraped to generate wounds before incubation with icaritin or DMSO control for 12 h in the absence of serum, with representative serial images captured at 0, 6 and 12 h. (B) Quantitative analysis of the scratch wound healing assay calculated by the wound width (pixel) over time (*: $p < 0.05$, $n = 4$).

handling quadrupedal SAON rabbit model [10,24].

Large bipedal emu was chosen due to its suitability for orthopaedic and biomaterial research as a large bipedal animal model suitable for studying SAON in a pre-clinical setting [23]. MR imaging confirmed that SAON occurred 12 weeks post-induction in emus. At this stage, an abnormal gait similar to that seen in patients at stage I or stage II ON would be developed [48,49]. We undertook CD as a surgical intervention for studying the effect of P/T/I scaffold as bone defect filler after CD on prevention of femoral head collapse. The significantly lower incidence of femoral head collapse in P/T/I group suggests its potential for clinical trial studies and a wide range of clinical applications in the future.

Bone repair in emus with SAON after CD surgery was rigorously investigated to uncover the different aspects of bone healing. More new bone formation in the bone tunnel, consistently demonstrated by micro-CT and histology, was found in P/T/I group reflecting the osteopromotive effect of the bioactive molecular icaritin. This agrees with our previous study on a SAON rabbit model that showed both P/T and P/T/I scaffolds promoted bone repair, but with better treatment efficacy or promotive effect of P/T/I on bone repair than that of P/T [18,50]. The maximum strength and energy of ROI in the bone tunnel of P/T/I group suggested that the addition of icaritin yielded the best new bone regeneration potential to partially restore the mechanical stability of the defect. The fracture load estimation by micro-FEA revealed that the femoral head of P/T/I group could resist the largest strength. The greatly improved mechanical properties seen in P/T/I group can be explained by the better quality of new bone as assessed by micro-CT and histology.

Degeneration of the articular cartilage was found to be associated with femoral head ON and collapse of femoral head [51]. Articular cartilage degeneration might also be related to development of SAON under similar mechanisms, where ischemia, edema and adipogenesis in the subchondral bone could cause pathological changes in microenvironment of the articular cartilage, leading to decreased collagen synthesis and increased apoptosis of chondrocytes [52,53] and therefore cartilage thinning that ultimately aggravating femoral head collapse. Compared with the thickness of the articular cartilage in normal healthy emus reported in our earlier study [23], the cartilage of the SAON emus in all three groups were all significantly thinner, especially at the collapsed region. However, P/T/I scaffold still performed the best in supporting the local mechanical and biological environment so as to maintain the thickness of articular cartilage of the involved joints. The ultrasound indentation test of the present study showed that P/T/I scaffold indeed helped maintained stiffness of the articular cartilage. In addition, the histomorphological results showed that P/T/I scaffold could help preserved structural composition of the articular cartilage through the osteopromotive effects of icaritin. As articular cartilage protected the subchondral bone from excessive stress, the relatively preserved cartilage in P/T/I group could prevent articular surface collapse in this group.

MSCs homeostasis is vital for bone development and repair. Recently, it has been advocated that SAON may be a disease of bone cells and/or MSCs. The osteogenic ability of MSCs is decreased during early SAON development [54,55]. MSCs are multipotent

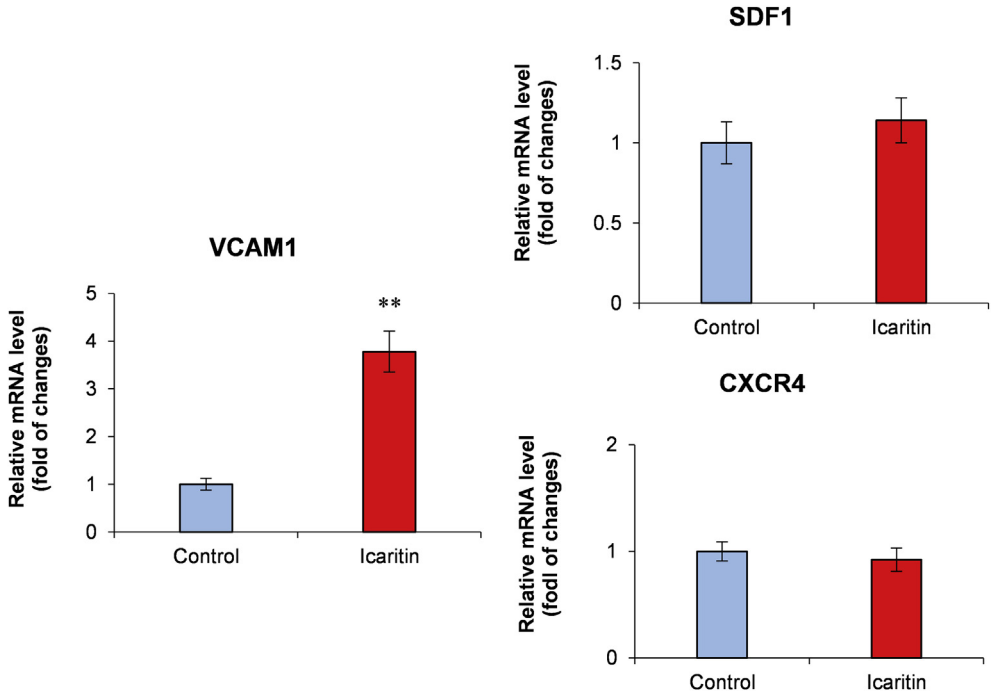


**Fig. 15.** Effect of Icaritin on BMSCs mRNA expression of migration related factors mRNA expression. RT-qPCR data on the migration related genes CXCR4, SDF1 and VCAM1 of rabbit BMSCs treated with ($10^{-6}$ M) or without icaritin for 24 h ($n = 3$). **: $p < 0.01$ for comparison between control and icaritin group.

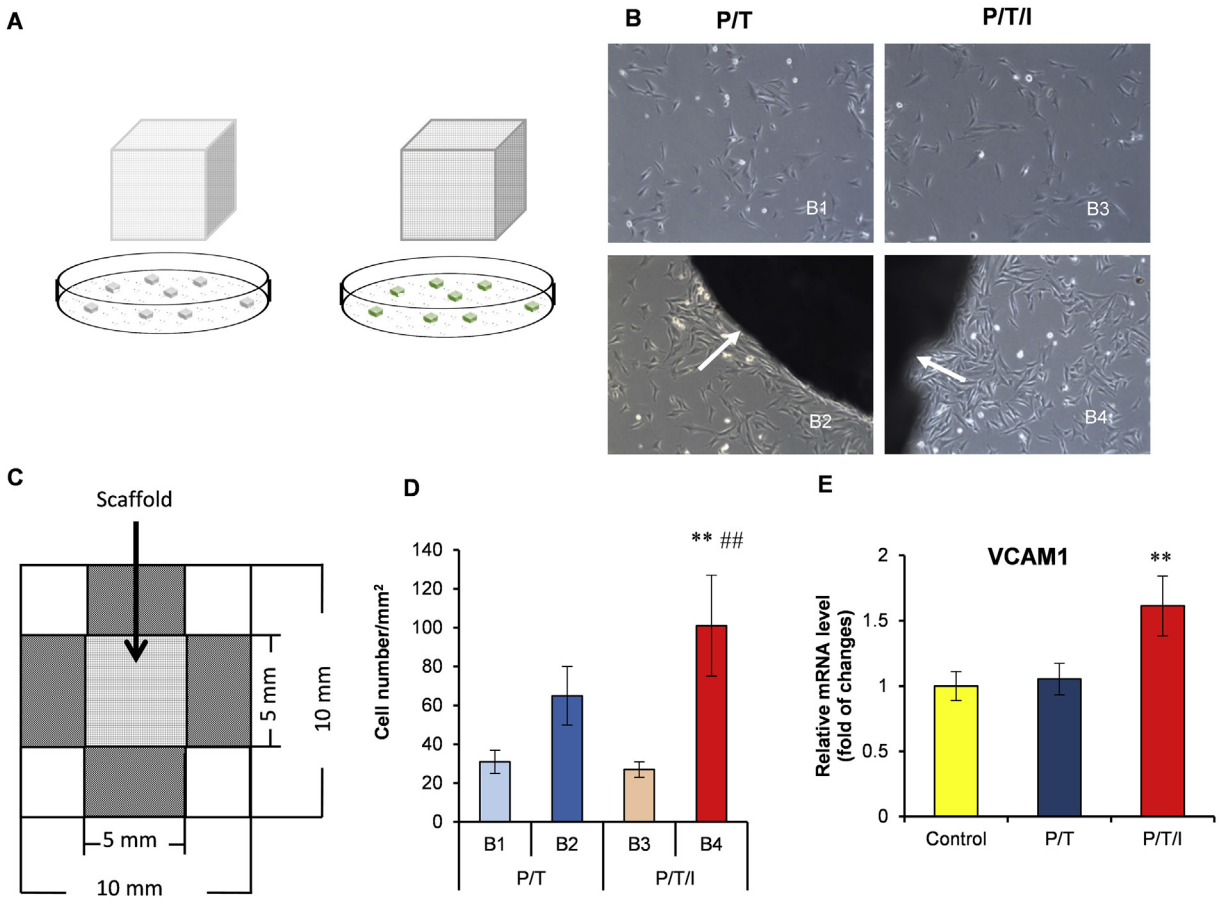


**Fig. 16.** P/T and P/T/I scaffolds on BMSCs recruitment *in vitro* (n = 4). (A) Schematic presentation of BMSCs cultured with P/T and P/T/I scaffolds. (B) Representative images taken at 24 h after culturing scaffolds with BMSCs. (B1&B2) For regions without and with scaffold in P/T group, and (B3&B4) for regions without and with scaffold in P/T/I group, respectively (white arrow: cells migrating into pores of the scaffold, 10×). (C) Schematic diagram for the four defined regions (dark check-pattern each of 2.5 × 5 $mm^2$) for counting cell number next to the edge of scaffold. (D) Quantitative comparison of cell number as specified in (B) and (C). ** and ##: $p < 0.01$) for comparison between different regions (B2 vs. B1 or B4 vs. B3) and between groups (P/T vs. P/T/I), respectively. (E) RT-qPCR data on the migration related gene VCAM1 of BMSCs cultured with P/T or P/T/I scaffold with standard tissue culture treated surface as the control. **:$p < 0.01$for comparison between P/T/I group and control group.

stromal cells which have the potential to differentiate into osteoblasts, adipocytes and other cell types. As corticosteroids promoted adipogenesis and inhibited osteogenesis, *in vitro* and *in vivo*, so that unbalanced differentiation of MSCs might lead to osteonecrosis as reported by others [56].

In this study, we found that icaritin could promote ALP activity, ALP expression and calcium nodules deposition of BMSCs from SAON (−) rabbits, suggesting that icaritin promoted osteogenic differentiation of BMSCs for new bone formation or regeneration. Furthermore, icaritin partially recovered the declined osteogenic potential of BMSCs in SAON (+) group. Our present work has clearly shown that icaritin can promote osteogenesis during bone repair in SAON. Lipid accumulation in SAON was most likely due to the increased adipocytic differentiation of MSCs. Icaritin decreased lipid accumulation in both SAON (−) and SAON (+) groups, demonstrating that it could inhibit adipogenesis during bone repair with SAON. The enhancement of osteogenesis and inhibition of adipogenesis of MSCs by icaritin with rabbit BMSCs demonstrated its beneficial effect on bone defect repair *in vitro* and this can be translated to other SAON animal models *in vivo*.

In order to understand the mechanism of icaritin on osteogenesis of MSCs, the expression of osteoblastic regulatory and marker genes BMP-2, RUNX2, COL1α and OC was determined. Over the years, many research studies have shown that corticosteroids lead to down-regulation of BMP-2, RUNX2, COL1α and OC expression of BMSCs *in vitro* and *in vitro* using various animal models [22,57–59]. BMP-2 is an early osteogenic gene that modulates the promoter region of RUNX2/Cbfa1. OC is a late osteogenic gene, and suppression of BMP-2 gene expression theoretically leads to a direct decrease of OC [60]. Therefore, BMP-2 serves as the main gene affected by steroids to suppress the osteogenesis in SAON. In this study, the decrease of expression of these osteogenic markers of BMSCs from SAON (+) rabbit compared to SAON (−) rabbit reconfirmed our SAON model in agreement with other studies. Icaritin promoted the expression of genes of BMSCs suggested that BMP-2 signaling pathway was involved in icaritin-mediated osteogenesis promotion [61].

Adipogenic markers aP2 and PPAR-γ were known to be upregulated in SAON [9,57,62], together with C/EBP, the mRNA expression of these three markers was of interest for us to confirm such an effect of icaritin. The increase in expression of these markers in SAON (+) showed that corticosteroid improved adipogenesis through C/EBP and PPAR-γ signaling pathways. C/EBPs belong to the basic-leucine zipper class of transcription factors which have been implicated in the induction of adipocyte differentiation [63]. C/EBPs are expressed before the transcription of most adipocyte-specific genes initiated and contribute to the subsequent induction of the major adipogenic transcription factors, including PPAR-γ

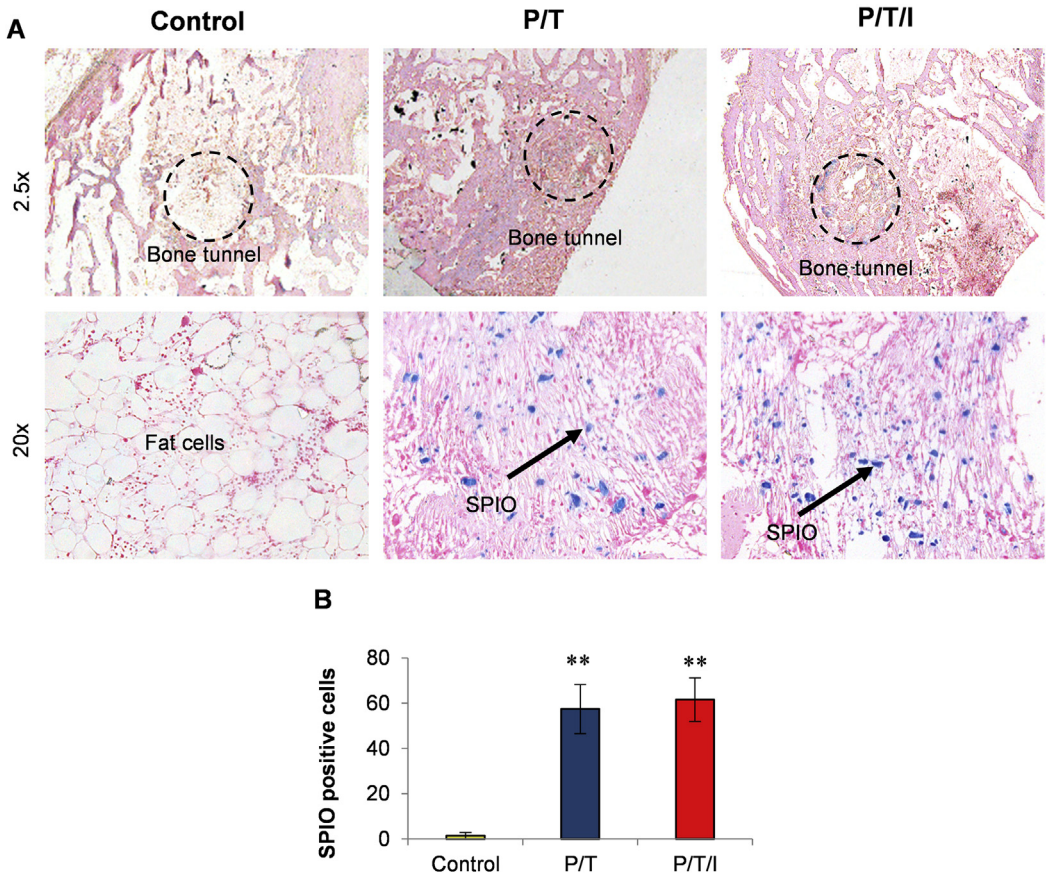


**Fig. 17.** Representative histology of rabbit femur at week 2 after scaffolds implantation and SPIO labeled BMSCs injection. (A) Prussian blue and nuclear fast red staining of the histological sections of empty control, P/T and P/T/I groups. The location of the bone tunnel was marked with a dotted circle (upper, 2.5×); SPIO positive cells were indicated by black arrows (lower, 20×). (B) SPIO positive cells on the histological sections were counted (n = 6) and plotted. **: $p < 0.01$ compared between P/T/I or P/T group and empty control group.

[64]. In particular, C/EBPs and C/EBP-β stimulate PPAR-γ activity by controlling the production of PPAR-γ ligand, and phosphorylation of C/EBP-β is required for PPAR-γ-associated downstream proteins involved in adipogenesis [65]. aP2 is expressed during adipocyte differentiation that has been regarded as a terminal differentiation marker [66]. PPAR-γ is the key transcription factor in adipocyte differentiation and plays an anti-osteoblastogenic role as the master regulator of adipogenesis [67]. After icaritin treatment, a significant inhibition of adipogenic differentiation appeared both in SAON (−) and SAON (+) groups. Western blot results further confirmed that icaritin inhibited PPAR-γ and aP2 expression at protein level. This suggested that icaritin inhibited adipogenesis of BMSCs through PPAR-γ-mediated pathway.

Whether P/T and/or P/T/I scaffolds promoted bone defect repair in SAON animal model via regulating stem cell homing, a fundamental mechanism on osteogenesis and potentially also angiogenesis/neovascularization, during bone defect repair in SAON rabbit was further investigated in this study. The migration of MSCs plays an important role in organogenesis during development and tissue repair. Regulation of MSCs homing from an endogenous niche or following systemic administration to the targeted region is critical for effective tissue regeneration. The homed MSCs were reported not only to be able to offer themselves for tissue regeneration but also serve as vehicles for *in vivo* delivery of therapeutic genes or factors to promote repair [68]. So a strategy for bone defect treatment shall not only facilitate osteogenesis and angiogenesis, but also trigger stem cell homing. In the SAON rabbit model, both P/T and P/T/I scaffolds were shown to promote SPIO labeled MSCs homing to bone defect region after CD surgery for enhancing bone defect repair. As a void filler and drug carrier, P/T scaffold itself was demonstrated to be effective in recruiting BMSCs migration. On the other hand, not only icaritin alone upregulated VCAM1 gene of BMSCs *in vitro*, but its bioactivity was also well preserved in P/T/I to upregulate VCAM1 *in vitro* and promote SPIO labeled BMSCs migration to bone defect region in SAON rabbit model. VCAM1 plays an important role in cell–cell recognition, through interacting with the beta-1 integrin very late antigen-4 (VLA4), by mediating both cell adhesion and signal transduction [69]. VCAM1 is involved in homing at the adhesion stage while VLA-4/VCAM-1 expressed by MSCs interacts with endothelial cells to promote firm adhesion of MSCs on endothelial surface and transmigration across the endothelium [70,71]; chemokines, e.g. SDF1, may further chemoattract MSCs from bone marrow to the injured tissue for repair enhancement [72]. SDF1 is mainly expressed by stromal and endothelial cells, and CXCR4 is a specific receptor for SDF1. The lack of effect of icaritin on CXCR4/SDF1 demonstrated that probably other migration-stimulating factors, in addition to VCAM-1, other than SDF1 were involved in mediating the stimulatory response of icaritin on BMSCs.

Since the prospect of icaritin as a novel osteogenic factor for stimulating bone regeneration was well demonstrated, we incorporated this anabolic phytomolecule icaritin into an

osteoconductive biomaterial P/T to form P/T/I scaffold to explore its treatment efficacy for SAON associated joint collapse using our recently established bipedal emu model. However, it was critical at the outset to ensure a sustained release of icaritin from the P/T/I scaffold. We previously reported the sustainable release of about 72% icaritin from a P/T/I scaffold over a period of 12 weeks and our findings supported that the P/T scaffold was an appropriate carrier for local icaritin delivery [22]. In addition, this scaffold also showed good biocompatibility and facilitated MSCs adhesion and ingrowth, which are the essential underlying mechanism on promoting osteogenesis [17,25]. In our recent study using an SAON rabbit model, both P/T and P/T/I scaffold showed bone healing enhancement yet with better osteopromotive effect in P/T/I scaffold [22]. The results from the current study also confirmed that icaritin could be successfully incorporated into P/T and maintained its bioactivity for enhancing bone defect repair healing in such a large bipedal emu model that was explained at least in part by its effects on attracting migration of BMSCs from remote region to the bone defect using a cost-effective rabbit model.

One of the limitations of the current study design was that two different animal models were used for exploring treatment efficacy and its mechanism. For bipedal animal model, emu has a body size close to that of humans suitable for testing orthopaedic biomaterials, but emu is also a large and expensive animal model for pre-clinical research. We demonstrated SAON-induced hip joint collapse in emu [23] that was explained by higher body to lower-limb weight ratio, i.e. higher mechanical loading imposed to the hip joint, which can only be induced in bipedal animal model such as emu [73,74]. On the contrary, rabbit SAON model is a well-established, cost effective and easy-handling one yet never shows hip joint collapse due to its quadrupedal nature with body weight distribution on four limbs. However, rabbits have metabolic pathway and bone density and structure more similar to humans than aves [75,76]. Taken together, we selected rabbits for studying the underlying mechanism of a 3-D bioactive scaffold containing an osteopromotive phytomolecule icaritin (P/T/I scaffold) at cellular and molecular level apart from limited availability of relevant antibodies and gene sequences for emu research. Although P/T/I scaffold was shown to promote BMSCs migration much better than P/T scaffold *in vitro*, the difference of these two scaffolds on the migration of SPIO labeled BMSCs *in vivo* was not obvious. This finding might be explained by an insufficient cell number and sample size for quantitative analysis, more likely that the unlabeled yet significant host circulating and local MSCs might have fundamentally contributed to the better treatment effects of P/T/I scaffold for bone defect repair in the current study.

## 5. Conclusion

In conclusion, we tested porous composite scaffold P/T incorporating an osteopromotive phytomolecule icaritin (P/T/I scaffold) that showed as an effective bone filler for promoting bone defect repair and prevention of hip joint collapse in bipedal SAON emu model. This effect was explained by its ability to promote MSC migration to the bone defect region for enhancing osteogenesis and inhibiting adipogenesis, indicating P/T/I scaffold as a 3-D printed bioactive scaffold for potential orthopaedic applications involving large bone defect repair.

## Conflicts of interest

All authors declare that there is no conflict of interest regarding the materials discussed in the manuscript.

## Funding/support

This work was supported by Hong Kong Innovation and Technology Commission (ITF Tier 2 – GHP/001/08; ITS/451/09FP), Hong Kong Research Grants Council (GRF CUHK-4737/10), NSFC-DG-RTD Joint Scheme (Project No. 51361130034) and the European Union's 7th Framework Programme (NMP-2013-EU-China Project No. 604517).

## Acknowledgment

The authors would like to thank Vivian Hung and Yixin He for their assistance in HR-pQCT scanning and sample preparation, and Ge Zhang, who currently works at School of Chinese Medicine of Hong Kong Baptist University for their initial involvement in the joint development of emu SAON model (in Zheng LZ et al. PLoS One 2013).

## Appendix A. Supplementary data

Supplementary data related to this article can be found at http://dx.doi.org/10.1016/j.biomaterials.2015.04.038.

## References

[1] Y. Assouline-Dayan, C. Chang, A. Greenspan, Y. Shoenfeld, M.E. Gershwin, Pathogenesis and natural history of osteonecrosis, Seminars Arthritis Rheum. 32 (2002) 94–124.
[2] M.H. Chan, P.K. Chan, J.F. Griffith, I.H. Chan, L.C. Lit, C.K. Wong, et al., Steroid-induced osteonecrosis in severe acute respiratory syndrome: a retrospective analysis of biochemical markers of bone metabolism and corticosteroid therapy, Pathology 38 (2006) 229–235.
[3] M.A. Mont, L.C. Jones, D.S. Hungerford, Nontraumatic osteonecrosis of the femoral head: ten years later, J. Bone Jt. Surg. Am. Volume 88 (2006) 1117–1132.
[4] C. Powell, C. Chang, S. Naguwa, G. Cheema, M. Gershwin, Steroid induced osteonecrosis: an analysis of steroid dosing risk, Autoimmun Rev. 9 (2010) 721–743.
[5] K. Ikeuchi, Y. Hasegawa, T. Seki, Y. Takegami, T. Amano, N. Ishiguro, Epidemiology of nontraumatic osteonecrosis of the femoral head in Japan, Mod Rheumatol. (2014) 1–4.
[6] C.C. Mok, C.S. Lau, R.W. Wong, Risk factors for avascular bone necrosis in systemic lupus erythematosus, Br. J. Rheumatol. 37 (1998) 895–900.
[7] National Center for Health Statistics, Health, United States, 2013: With Special Feature on Prescription Drugs, 2014. Hyattsville, MD.
[8] H. Mankin, Nontraumatic necrosis of bone (Osteonecrosis), N. Engl. J. Med. 326 (1992) 1473–1479.
[9] H. Sheng, G. Zhang, W. Cheung, C. Chan, Y. Wang, K. Lee, et al., Elevated adipogenesis of marrow mesenchymal stem cells during early steroid-associated osteonecrosis development, J. Orthop. Surg. Res. 2 (2007) 15.
[10] X. Xie, X. Wang, G. Zhang, Z. Liu, D. Yao, L. Hung, et al., Impaired bone healing in rabbits with steroid-induced osteonecrosis, J. Bone Jt. Surg. Br. 93 (2011) 558–565.
[11] G. Zhang, L. Qin, Y. Shi, Epimedium-derived phytoestrogen flavonoids exert beneficial effect on preventing bone loss in late postmenopausal women: a 24-month randomized, double-blind and placebo-controlled trial, J. Bone Mineral Res. Official J. Am. Soc. Bone Mineral Res. 22 (2007) 1072–1079.
[12] H.M. Zhu, L. Qin, P. Garnero, H.K. Genant, G. Zhang, K. Dai, et al., The first multicenter and randomized clinical trial of herbal Fufang for treatment of postmenopausal osteoporosis, Osteoporos. Int. J. Established Result Coop. Eur. Found. Osteoporos. Natl. Osteoporos. Found. U. S. A 23 (2012) 1317–1327.
[13] G. Zhang, L. Qin, H. Sheng, X.L. Wang, Y.X. Wang, D.K. Yeung, et al., A novel semisynthesized small molecule icaritin reduces incidence of steroid-associated osteonecrosis with inhibition of both thrombosis and lipid-deposition in a dose-dependent manner, Bone 44 (2009) 345–356.
[14] D. Yao, X.H. Xie, X.L. Wang, C. Wan, Y.W. Lee, S.H. Chen, et al., Icaritin, an exogenous phytomolecule, enhances osteogenesis but not angiogenesis–an in vitro efficacy study, PLoS One 7 (2012) e41264.
[15] B. Derby, Printing and prototyping of tissues and scaffolds, Science 336 (2012) 921–926.
[16] H. Kai, X. Wang, K. Madhukar, L. Qin, Y. Yan, R. Zhang, et al., Fabrication of a two-level tumor bone repair biomaterial based on a rapid prototyping technique, Biofabrication 1 (2009) 025003.
[17] S. Chen, X. Wang, X. Xie, L. Zheng, D. Yao, D. Wang, et al., Comparative study of osteogenic potential of a composite scaffold incorporating either endogenous bone morphogenetic protein-2 or exogenous phytomolecule icaritin: an in vitro efficacy study, Acta Biomater 8 (2012) 3128–3137.

[18] C. Chen, L. Zheng, X. Xie, M. Lei, X. Wang, Y. Lai, et al., Comparative study of PLGA/TCP scaffolds incorporated or coated with osteogenic growth factors for enhancement of bone regeneration, J. Orthop. Transl. 2 (2014) 91–104.
[19] C.H. Lee, J.L. Cook, A. Mendelson, E.K. Moioli, H. Yao, J.J. Mao, Regeneration of the articular surface of the rabbit synovial joint by cell homing: a proof of concept study, Lancet 376 (2010) 440–448.
[20] B. Stevens, Y. Yang, A. Mohandas, B. Stucker, K. Nguyen, A review of materials, fabrication methods, and strategies used to enhance bone regeneration in engineered bone tissues, J. Biomed. Mater. Res. B Appl. Biomater. 85 (2008) 573–582.
[21] S. Chen, M. Lei, X. Xie, L. Zheng, D. Yao, X. Wang, et al., PLGA/TCP composite scaffold incorporating bioactive phytomolecule icaritin for enhancement of bone defect repair in rabbits, Acta Biomater. 9 (2013) 6711–6722.
[22] X. Wang, X. Xie, G. Zhang, S. Chen, D. Yao, K. He, et al., Exogenous phytoestrogenic molecule icaritin incorporated into a porous scaffold for enhancing bone defect repair, J. Orthop. Res. 31 (2012) 164–172.
[23] L. Zheng, Z. Liu, M. Lei, J. Peng, Y. He, X. Xie, et al., Steroid-associated hip joint collapse in bipedal emus, PLoS One 8 (2013) e76797.
[24] L. Qin, G. Zhang, H. Sheng, K. Yeung, H. Yeung, C. Chan, et al., Multiple bioimaging modalities in evaluation of an experimental osteonecrosis induced by a combination of lipopolysaccharide and methylprednisolone, Bone 39 (2006) 863–871.
[25] X. Xie, X. Wang, G. Zhang, Y. He, X. Wang, Z. Liu, et al., Structural and degradation characteristics of an innovative porous PLGA/TCP scaffold incorporated with bioactive molecular icaritin, Biomed. Mater. 5 (2010) 054109.
[26] M.H. Lu, Y.P. Zheng, H.B. Lu, Q.H. Huang, L. Qin, Evaluation of bone-tendon junction healing using water jet ultrasound indentation method, Ultrasound Med. Biol. 35 (2009) 1783–1793.
[27] M. Lu, Y. Zheng, Q. Huang, C. Ling, Q. Wang, L. Bridal, et al., Noncontact evaluation of articular cartilage degeneration using a novel ultrasound water jet indentation system, Ann. Biomed. Eng. 37 (2009) 164–175.
[28] X.H. Xie, X.L. Wang, G. Zhang, Z. Liu, D. Yao, L.K. Hung, et al., Impaired bone healing in rabbits with steroid-induced osteonecrosis, J Bone Jt. Surg. 93 (2010) 558–565.
[29] X.H. Xie, X.L. Wang, Y.X. He, Z. Liu, H. Sheng, G. Zhang, et al., Promotion of bone repair by implantation of cryopreserved bone marrow-derived mononuclear cells in a rabbit model of steroid-associated osteonecrosis, Arthritis Rheum. 64 (2012) 1562–1571.
[30] B. van Rietbergen, H. Weinans, R. Huiskes, A. Odgaard, A new method to determine trabecular bone elastic properties and loading using micromechanical finite-element models, J. Biomech. 28 (1995) 69–81.
[31] K.L. Reed, T.D. Brown, Elastic modulus and strength of emu cortical bone, Iowa Orthop. J. 21 (2001) 53–57.
[32] C.H. Turner, J. Rho, Y. Takano, T.Y. Tsui, G.M. Pharr, The elastic properties of trabecular and cortical bone tissues are similar: results from two microscopic measurement techniques, J. Biomech. 32 (1999) 437–441.
[33] D.T. Reilly, A.H. Burstein, V.H. Frankel, The elastic modulus for bone, J. Biomech. 7 (1974) 271–275.
[34] J.Y. Rho, T.Y. Tsui, G.M. Pharr, Elastic properties of human cortical and trabecular lamellar bone measured by nanoindentation, Biomaterials 18 (1997) 1325–1330.
[35] T.M. Keaveny, P.F. Hoffmann, M. Singh, L. Palermo, J.P. Bilezikian, S.L. Greenspan, et al., Femoral bone strength and its relation to cortical and trabecular changes after treatment with PTH, alendronate, and their combination as assessed by finite element analysis of quantitative CT scans, J. Bone Min. Res. 23 (2008) 1974–1982.
[36] W. Pistoia, B. van Rietbergen, E.M. Lochmuller, C.A. Lill, F. Eckstein, P. Ruegsegger, Estimation of distal radius failure load with micro-finite element analysis models based on three-dimensional peripheral quantitative computed tomography images, Bone 30 (2002) 842–848.
[37] I. Acta BiomaterialiaKiviranta, J. Jurvelin, M. Tammi, A.M. Saamanen, H.J. Helminen, Microspectrophotometric quantitation of glycosaminoglycans in articular cartilage sections stained with Safranin O, Histochemistry 82 (1985) 249–255.
[38] K.S. Leung, L. Qin, M.C. Leung, L.L. Fu, C.W. Chan, Partial patellectomy induces a decrease in the proteoglycan content in the remaining patellar articular cartilage. An experimental study in rabbits, Clin. Exp. Rheumatol. 17 (1999) 597–600.
[39] L. Qin, L. Wang, M.W. Wong, C. Wen, G. Wang, G. Zhang, et al., Osteogenesis induced by extracorporeal shockwave in treatment of delayed osteotendinous junction healing, J. Orthop. Res. 28 (2010) 70–76.
[40] S.C. Miller, T.H. Omura, L.J. Smith, Changes in dentin appositional rates during pregnancy and lactation in rats, J. Dent. Res. 64 (1985) 1062–1064.
[41] K.R. Brunt, S.R. Hall, C.A. Ward, L.G. Melo, Endothelial progenitor cell and mesenchymal stem cell isolation, characterization, viral transduction, Methods Mol. Med. 139 (2007) 197–210.
[42] D. Yao, X.H. Xie, X.L. Wang, C. Wan, Y.W. Lee, S.H. Chen, et al., Icaritin, an exogenous phytomolecule, enhances osteogenesis but not angiogenesis-an in vitro efficacy study, PLoS One 7 (2012) e41264.
[43] B. Chan, S. Fu, L. Qin, K. Lee, C. Rolf, K. Chan, Effects of basic fibroblast growth factor (bFGF) on early stages of tendon healing: a rat patellar tendon model, Acta Orthop. Scand 71 (2000) 513–518.
[44] H.H. Wang, Y.X. Wang, K.C. Leung, D.W. Au, S. Xuan, C.P. Chak, et al., Durable mesenchymal stem cell labelling by using polyhedral superparamagnetic iron oxide nanoparticles, Chemistry 15 (2009) 12417–12425.
[45] Y.X. Wang, K.C. Leung, W.H. Cheung, H.H. Wang, L. Shi, D.F. Wang, et al., Low-intensity pulsed ultrasound increases cellular uptake of superparamagnetic iron oxide nanomaterial: results from human osteosarcoma cell line U2OS, J Magnetic Reson. Imaging: JMRI 31 (2010) 1508–1513.
[46] L. Qin, G. Zhang, H. Sheng, K.W. Yeung, H.Y. Yeung, C.W. Chan, et al., Multiple bioimaging modalities in evaluation of an experimental osteonecrosis induced by a combination of lipopolysaccharide and methylprednisolone, Bone 39 (2006) 863–871.
[47] G.M. van Buul, G. Kotek, P.A. Wielopolski, E. Farrell, P.K. Bos, H. Weinans, et al., Clinically translatable cell tracking and quantification by MRI in cartilage repair using superparamagnetic iron oxides, PLoS One 6 (2011) e17001.
[48] J.W.M. Gardeniers, ARCO Committee on Terminology and Staging.The ARCO perspective for reaching one uniform staging system of osteonecrosis, in: A. Schoutens, J. Arlet, J.W.M. Gardeniers, S.P.F. Hughes (Eds.), Bone Circulation and Vascularization in Normal and Pathological Conditions, Plenum Press, New York, 1993, pp. 375–380.
[49] A.H. Zibis, A.H. Karantanas, N.T. Roidis, M.E. Hantes, P. Argiri, T. Moraitis, et al., The role of MR imaging in staging femoral head osteonecrosis, Eur. J. Radiol. 63 (2007) 3–9.
[50] X.L. Wang, X.H. Xie, G. Zhang, S.H. Chen, D. Yao, K. He, et al., Exogenous phytoestrogenic molecule icaritin incorporated into a porous scaffold for enhancing bone defect repair, J. Orthop. Res. 31 (2012) 164–172.
[51] J. McCarthy, L. Puri, W. Barsoum, J.A. Lee, M. Laker, P. Cooke, Articular cartilage changes in avascular necrosis: an arthroscopic evaluation, Clin. Orthop. Relat. Res. (2003) 64–70.
[52] S. Fubini, R. Todhunter, N. Burton-Wurster, M. Vernier-Singer, J. MacLeod, Corticosteroids alter the differentiated phenotype of articular chondrocytes, J. Orthop. Res. 19 (2001) 688–695.
[53] B. Farkas, K. Kvell, T. Czömpöly, T. Illés, T. Bárdos, Increased chondrocyte death after steroid and local anesthetic combination, Clin. Orthop. Relat. Res. 468 (2010) 3112–3120.
[54] H.H. Sheng, G.G. Zhang, W.H. Cheung, C.W. Chan, Y.X. Wang, K.M. Lee, et al., Elevated adipogenesis of marrow mesenchymal stem cells during early steroid-associated osteonecrosis development, J. Orthop. Surg. Res. 2 (2007) 15.
[55] L.I. Plotkin, S.C. Manolagas, T. Bellido, Glucocorticoids induce osteocyte apoptosis by blocking focal adhesion kinase-mediated survival. Evidence for inside-out signaling leading to anoikis, J. Biol. Chem. 282 (2007) 24120–24130.
[56] C. Powell, C. Chang, M.E. Gershwin, Current concepts on the pathogenesis and natural history of steroid-induced osteonecrosis, Clin. Rev. Allergy Immunol. 41 (2011) 102–113.
[57] Q. Cui, G. Wang, G. Balian, Steroid-induced adipogenesis in a pluripotential cell line from bone marrow, J. Bone Jt. Surg. Am. 79 (1997) 1054–1063.
[58] J. Chang, M. Ho, C. Yeh, C. Chen, G. Wang, Osteogenic gene expression decreases in stromal cells of patients with osteonecrosis, Clin. Orthop. Relat. Res. 453 (2006) 286–292.
[59] X. Li, J. Bai, X. Ji, R. Li, Y. Xuan, Y. Wang, Comprehensive characterization of four different populations of human mesenchymal stem cells as regards their immune properties, proliferation and differentiation, Int. J. Mol. Med. 34 (2014) 695–704.
[60] W. Jang, E. Kim, D. Kim, H. Ryoo, K. Lee, S. Kim, et al., BMP2 protein regulates osteocalcin expression via Runx2-mediated Atf6 gene transcription, J. Biol. Chem. 287 (2012) 905–915.
[61] D. Yao, X. Xie, X. Wang, C. Wan, Y. Lee, S. Chen, et al., Icaritin, an exogenous phytomolecule, enhances osteogenesis but not angiogenesis–an in vitro efficacy study, PLoS One 7 (2012) e41264.
[62] W. Wang, L. Liu, X. Dang, S. Ma, M. Zhang, K. Wang, The effect of core decompression on local expression of BMP-2, PPAR-γ and bone regeneration in the steroid-induced femoral head osteonecrosis, BMC Musculoskelet Disord 13 (2012) 142.
[63] S. Mandrup, M.D. Lane, Regulating adipogenesis, J. Biol. Chem. 272 (1997) 5367–5370.
[64] L. Fajas, J.C. Fruchart, J. Auwerx, Transcriptional control of adipogenesis, Curr. Opin. Cell Biol. 10 (1998) 165–173.
[65] S.R. Farmer, Regulation of PPARgamma activity during adipogenesis, Int. J. Obes (Lond) 29 (suppl. 1) (2005) S13–S16.
[66] L. Sun, A.C. Nicholson, D.P. Hajjar, A.M. Gotto Jr., J. Han, Adipogenic differentiating agents regulate expression of fatty acid binding protein and CD36 in the J744 macrophage cell line, J. Lipid Res. 44 (2003) 1877–1886.
[67] M. Kawai, C.J. Rosen, PPARgamma: a circadian transcription factor in adipogenesis and osteogenesis, Nat. Rev. Endocrinol. 6 (2010) 629–636.
[68] N. Smart, P.R. Riley, The stem cell movement, Circ. Res. 102 (2008) 1155–1168.
[69] V.F. Segers, I. Van Riet, L.J. Andries, K. Lemmens, M.J. Demolder, A.J. De Becker, et al., Mesenchymal stem cell adhesion to cardiac microvascular endothelium: activators and mechanisms, Am. J. Physiol. 290 (2006) H1370–H1377.
[70] B. Ruster, S. Gottig, R.J. Ludwig, R. Bistrian, S. Muller, E. Seifried, et al., Mesenchymal stem cells display coordinated rolling and adhesion behavior on endothelial cells, Blood 108 (2006) 3938–3944.
[71] C. Steingen, F. Brenig, L. Baumgartner, J. Schmidt, A. Schmidt, W. Bloch, Characterization of key mechanisms in transmigration and invasion of mesenchymal stem cells, J. Mol. Cell Cardiol. 44 (2008) 1072–1841.
[72] X. Xu, F. Zhu, M. Zhang, D. Zeng, D. Luo, G. Liu, et al., Stromal cell-derived factor-1 enhances wound healing through recruiting bone marrow-derived

mesenchymal stem cells to the wound area and promoting neovascularization, Cells Tissues Organs 197 (2013) 103–113.
[73] M. Fan, J. Peng, A. Wang, L. Zhang, B. Liu, Z. Ren, et al., Emu model of full-range femoral head osteonecrosis induced focally by an alternating freezing and heating insult, J. Int. Med. Res. 39 (2011) 187–198.
[74] M. Conzemius, T. Brown, Y. Zhang, R. Robinson, A new animal model of femoral head osteonecrosis: one that progresses to human-like mechanical failure, J. Orthop. Res. 20 (2002) 303–309.
[75] M. Peric, I. Dumic-Cule, D. Grcevic, M. Matijasic, D. Verbanac, R. Paul, et al., The rational use of animal models in the evaluation of novel bone regenerative therapies, Bone 70 (2014) 73–86.
[76] J. Neyt, J. Buckwalter, N. Carroll, Use of animal models in musculoskeletal research, Iowa Orthop. J. 18 (1998) 118–123.